Cyclogenesis: Simulating Hurricanes and Tornadoes

JORGE ALEJANDRO AMADOR HERRERA, KAUST
JONATHAN KLEIN, KAUST
DAOMING LIU, KAUST
WOJTEK PAŁUBICKI, UAM
SÖREN PIRK, CAU
DOMINIK L. MICHELS, KAUST

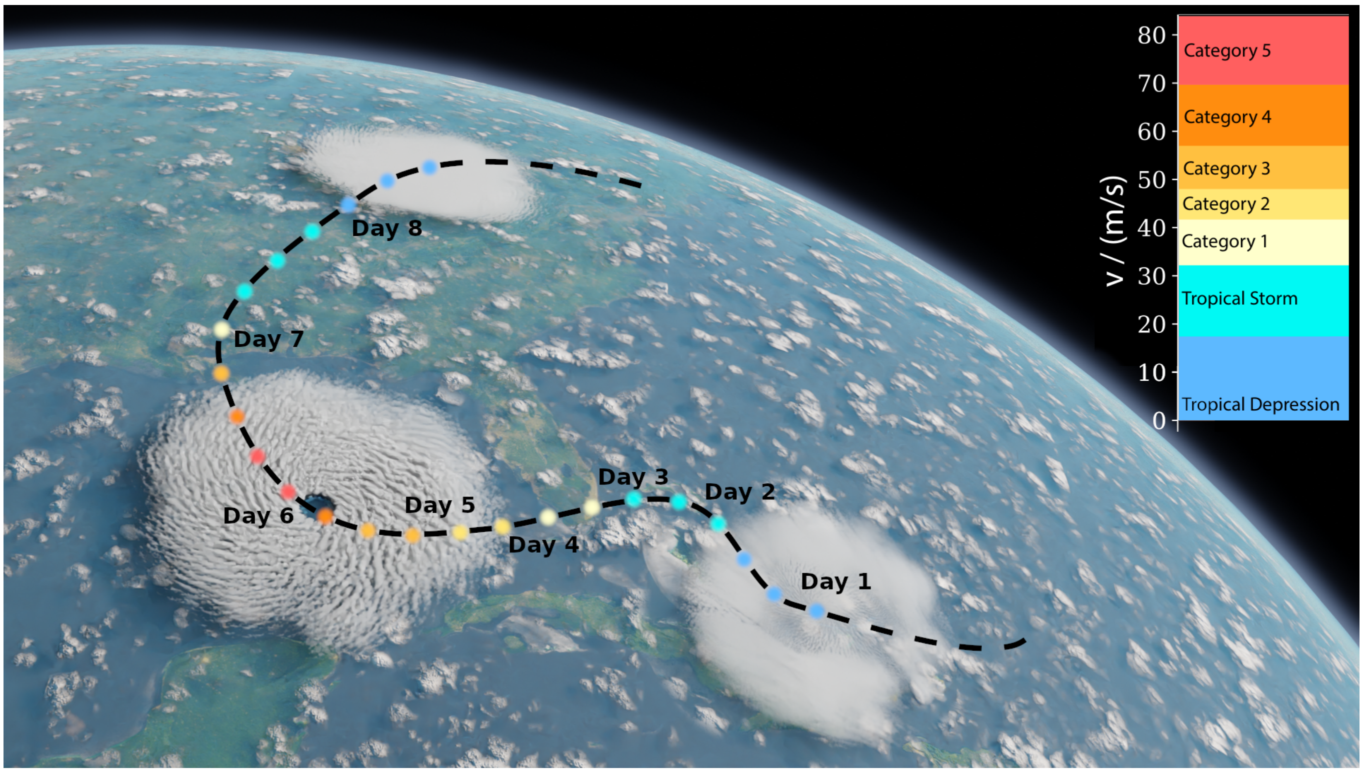

Fig. 1. Simulation of a hurricane forming over the Atlantic Ocean traveling through the Gulf of Mexico until it hits the US coast and starts decaying due to the lack of enough latent heat to sustain vorticity. The hurricane's trajectory is similar to the one of the category-5-hurricane *Katrina* which particularly hit the city of New Orleans and its surrounding area in 2005 causing over 1 300 fatalities and severe damage. The hurricane's intensity is color-coded along the trajectory according to the Saffir–Simpson scale [Taylor et al. 2010] ranging from a tropical depression to a category-5-hurricane (see top right corner).

Cyclones are large-scale phenomena that result from complex heat and water transfer processes in the atmosphere, as well as from the interaction of multiple *hydrometeors*, i.e., water and ice particles. When cyclones make landfall, they are considered natural disasters and spawn dread and awe alike. We propose a physically-based approach to describe the 3D development of cyclones in a visually convincing and physically plausible manner. Our approach allows us to capture large-scale heat and water continuity, turbulent microphysical dynamics of hydrometeors, and mesoscale cyclonic processes within the planetary boundary layer. Modeling these processes enables us to simulate multiple hurricane and tornado phenomena. We evaluate our simulations quantitatively by comparing to real data from storm soundings and observations of hurricane landfall from climatology research. Additionally, qualitative comparisons to previous methods are performed to validate the different parts of our scheme. In summary, our model simulates

This work was supported by KAUST through the baseline funding of the Computational Sciences Group within the Visual Computing Center.
Authors' addresses: Jorge Alejandro Amador Herrera, KAUST, Visual Computing Center, Thuwal 23955, KSA; Jonathan Klein, KAUST, Visual Computing Center, Thuwal 23955, KSA; Daoming Liu, KAUST, Visual Computing Center, Thuwal 23955, KSA; Wojtek Pałubicki, UAM, Umultowska 87, 61-614 Poznań, Poland; Sören Pirk, CAU, Christian-Albrechts-Platz 4, 24118 Kiel, Germany; Dominik L. Michels, KAUST, Visual Computing Center, Thuwal 23955, KSA.

0730-0301/2024/7-ART71
https://doi.org/10.1145/3658149

cyclogenesis in a comprehensive way that allows us to interactively render animations of some of the most complex weather events.

CCS Concepts: • **Computing methodologies** → **Physical simulation**.

Additional Key Words and Phrases: Cyclonic Phenomena, Fluid Simulation, Hurricanes, Tornadoes, Turbulence Modeling, Weather Phenomena.

ACM Reference Format:
Jorge Alejandro Amador Herrera, Jonathan Klein, Daoming Liu, Wojtek Pałubicki, Sören Pirk, and Dominik L. Michels. 2024. Cyclogenesis: Simulating Hurricanes and Tornadoes. *ACM Trans. Graph.* 43, 4, Article 71 (July 2024), 16 pages. https://doi.org/10.1145/3658149

1 INTRODUCTION

Cyclogenesis denotes the formation or strengthening of a low-pressure area that favors the formation of tropical cyclones. Such tropical cyclones are rapidly rotating storm systems that feature a low-pressure center, a closed low-level atmospheric circulation, and powerful winds. These storms are organized in a spiral pattern of thunderstorms with heavy rain and squalls. Depending on where they form and how strong they are, these storms may be referred to as "hurricanes" or "typhoons". Hurricanes are strong tropical cyclones that occur over the Atlantic or northeastern Pacific Ocean, while typhoons form in the northwestern Pacific Ocean.[1] Given the significance of cyclones as natural disasters and downright terrifying phenomena, they have received a considerable amount of scientific interest in a wide range of different fields of research. In climatology or meteorology, research has focused on mesoscale simulations employing statistical as well as principled approaches, e.g., Cui and Caracoglia [2019]. These simulations usually emphasize specific aspects of cyclonic phenomena but do not describe them comprehensively within an integrated model that includes changes in the diurnal cycle, microphysical processes, and dynamically changing boundary conditions. Moreover, these models require, in general, the use of supercomputers and specialized hardware and software architectures [Orf 2019]. This makes a direct application of these methods for visual computing applications unfeasible. In graphics, several research works were proposed towards modeling cloud formations and other weather phenomena, e.g., Amador Herrera et al. [2021], but none of these approaches consider the additional turbulent-flow processes that can develop into a hurricane.

In this paper, we propose a physically-based approach to describe the formation of cyclones. Our method explicitly models the turbulent microphysics which forms the basis of cyclogenesis by coupling different interacting hydrometeors: Cloud water, ice, rain, snow, and graupel (i.e., precipitated ice). Additionally, we incorporate a two-fluid model for tornadogenesis to describe the emergent development of vortex tubes which may form as a consequence of cyclonic dynamics. Finally, we introduce a mathematical model that captures the large-scale transfer of heat and vapor between water bodies and the atmosphere, which leads to the formation of hurricanes.

Our key contributions are: (1) We propose a comprehensive physically-based scheme for computing the turbulent transport of heat and water in the atmosphere, which includes the multi-scale simulation of vortex phenomena as well as two-fluid coupling for interacting dust and debris; (2) We close our turbulent-flow equations by formulating extended eddy mixing microphysics, modeling the interactions between ice and water particles; (3) We address the dynamics of the emergence, development, and dissipation of cyclonic phenomena at different scales, enabling the visually realistic and physically plausible simulation of these extreme weather events, as demonstrated by multiple validation and comparison experiments.

[1]In the Indian Ocean, South Pacific, or South Atlantic, these storms are simply called "tropical cyclones".

2 RELATED WORK

The modeling and simulation of cyclone dynamics and turbulent weather phenomena is an ongoing research topic in different academic communities. While this spans a breadth of work that we cannot conclusively discuss here, we provide references to the modeling and simulation of local weather, physical studies of tornadic phenomena, and the simulation of cyclogenesis at the mesoscale. Outside of visual computing, there have been multiple studies on different aspects of turbulent phenomena. Cyclogenesis within a storm has been studied in detail by Klemp [1987], and Rotunno and Klemp [1985]. Development of convection and general circulation at thunderstorm boundaries has been investigated by Droegemeier and Wilhelmson [1985]. On another direction, the role of latent heat on generating and sustaining vortexes has been studied numerically by Gao et al. [2019] and experimentally by Sheets [1982]. The goal of our work is to provide a comprehensive framework for the interactive simulation of turbulent weather dynamics at both the mesoscale and the storm-scale. In the following paragraphs, we will discuss related work.

Weather Simulation. One of the first methods for simulating clouds based on the underlying atmospheric phenoma was introduced by Kajiya and Von Herzen [1984]. Several interactive cloud simulation approaches have been proposed that range from grid-based fluid solvers [Dobashi et al. 2000; Harris et al. 2003; Miyazaki et al. 2002, 2001; Overby et al. 2002], particle-based approaches [Goswami and Neyret 2017] and methods based on GPU-parallelization [Schalkwijk et al. 2015]. To also enable artistic control of modeling clouds, procedural techniques have been proposed [Webanck et al. 2018]. Due to the complexity of simulating physics various representations have been explored that enable the efficient simulation and modeling of clouds and weather [Bouthors and Neyret 2004; Dobashi 2002; Gardner 1985; Neyret 1997; Nishita et al. 1996] including position-based dynamics [Ferreira Barbosa et al. 2015] and layer-based approaches [Vimont et al. 2020]. A common approach is to use hierarchical and adaptive grid structures to simulate the fluid dynamics for clouds [Raateland et al. 2022]. Other methods focus on large-eddy phenomena [Griffith et al. 2009], rain [Garcia-Dorado et al. 2017] and snow [Gissler et al. 2020], supercells [Hädrich et al. 2020], and complex weatherscapes [Amador Herrera et al. 2021]. It has been recognized that vegetation can contribute to local weather variations resulting in diverse microclimates [Pałubicki et al. 2022]. Furthermore, wildfires generating flammagenitus clouds have been simulated [Hädrich et al. 2021]. Despite these advances, it is important to note that none of these approaches consider a turbulent scheme, so cyclonic phenomena can only be prescribed but not simulated from first-principles.

Tornadic Phenomena. The work of Orf et al. [2017] achieved impressive results of tornadic phenomena within a supercell, including the formation, evolution and decay of multiple vortices. However, their scheme uses a supercomputer, billions of grid nodes and is far from being an interactive approach. A similar work [Orf 2019] uses grids of the order of trillions of nodes. The same holds true for other mesoscale frameworks where the focus is on processing precise physical data for comparison to storm soundings [Miglietta et al. 2017; Pilguj et al. 2019]. In the visual computing community, tornadoes have been simulated by Liu et al. [2006] whose model can generate visually convincing tornadoes but relies on prescribed rotational boundary conditions. Liu et al. [2007] improves the model by considering a reynolds averaging dynamics and coupling the tornado to destructive domains, but suffers from the same high dependence on boundary conditions. Also in these models the supercell is descriptively modeled and only the tornado (lower vortex tubes) is simulated emergently.

Cyclonic Modelling. Within the field of visual computing, cloud dynamics and weather phenomena in general have not been simulated on the hurricane scale. While the works of Hädrich et al. [2020] and Amador Herrera et al. [2021] do consider supercell formation and development, they only model the formation of a single cumulonimbus, and not a cluster of clouds that can evolve into a hurricane. Additionally, there is no work in the visual computing community that explicitly handles turbulence and cyclonic dynamics within a cloud scheme. In the atmospheric science community, multiple efforts have been made to study different aspects of cyclonic phenomena at the mesoscale from the stochastic generation and decay of hurricanes [Cui and Caracoglia 2019], the influence of latent heat in turbulent cumulus convection [Kuo 1965], dynamics of the energy budget within mesoscale storms [Peng and Kuo 1975], to the nonlinear dynamics of wind fields within typhoons [Vickery et al. 2000]. In the context of scientific visualizations, some works explore techniques for the interactive visual analysis of hurricane data [Doleisch et al. 2004], while other focus on developing educational visualizations of hurricanes [Luo et al. 2008]. Note, however, that the data for visualization in these works is not simulated, just taken *a priori*. In contrast to research in tornadic phenomena, works on turbulent dynamics associated to hurricanes tend to focus on analyzing specific aspects of cyclonic phenomena, as opposed to having a comprehensive framework for their simulation that includes diurnal cycles, ice-phase microphysics, and dynamic boundaries.

3 OVERVIEW

The principal motivation for our approach is to realistically model and simulate turbulent weather phenomena using a comprehensive scheme that can be used for graphics applications. This is a challenging task due to the complex interplay of heat and fluid dynamics within a turbulent wind field, as well as due to the presence of debris and mesoscale phenomena that determine the regional energy budget. We address these challenges by proposing an integrated physically-based model that targets the multi-scale simulation of turbulent heat and water transport in the atmosphere. As illustrated in Figure 2, our approach aims for a compromise between interactivity and physical complexity. Our framework empowers artists with interactive modeling control over a rich set of cyclonic phenomena.

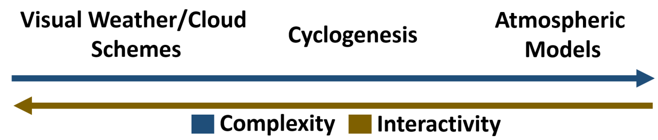

Fig. 2. Schematic representation of our *Cyclogenesis* framework in comparison to other visual weather/clouds schemes and atmospheric models. The complexity of our approach enables us to capture diverse cyclone phenomena not present in the state-of-the-art in visual computing. Being tailored for visual applications in mind, it does not require highly specialized supercomputer architectures, as atmospheric models typically do, boosting interactive practical usability for applications in graphics and beyond.

We describe the state of the atmosphere using five main quantities: the wind velocity $\boldsymbol{u}$, the velocity of dust in the air $\boldsymbol{u}_d$, the amount of water in the atmosphere q_a (in the form of vapor q_v, rain q_r, etc.), the temperature θ of humid air, and the turbulent energy k which sustains turbulent motion. At its core, our cyclogenesis model consists on coupling these quantities to capture the interplay of turbulent heat and water continuity. In this sense, our model can be divided into **(I)** a subgrid-energy scheme that describes enhanced transport due to turbulence, closure equations that incorporate the associated **(II)** turbulent microphysics and **(III)** Reynolds-Averaged Navier Stokes' dynamics, **(IV)** an extended Kesler-type approach to address turbulent heat and water dynamics, and **(V)** a two-fluid model that couples atmospheric and dust fields, as illustrated in Figure 3. Since hurricanes and tornadoes operate at different scales, we propose different set of equations (**III.1**) and (**IV.1**) for mesoscale cyclonic phenomena, which take into account the energy budget of water bodies, the axis-symmetrical nature of hurricanes, and the Coriolis effect.

4 METHODOLOGY

In this section, we provide an outline of our physics-based cyclogenesis model. It is a general and efficient scheme for the turbulent transport of heat and water in the atmosphere, including different *hydrometeors* or particles: vapor q_v, cloud water q_w, cloud ice q_i, rain q_r, snow q_s, and graupel q_g. For convenience, we use tensor notation for the derivation of our Reynolds-Average formulation. A brief explanation of this type of notation is presented in Appendix A.2. Additionally, a table of symbols, including the values used for our simulations, is provided in Appendix A.1.

4.1 Atmospheric Model

Our atmospheric scheme starts with a parameterization of the reference background atmosphere, as well as a thermodynamic model for the rising thermal of humid air.

4.1.1 Background Atmosphere. The surrounding dry air is parameterized in terms of its time-dependent temperature T and pressure fields p in space $\boldsymbol{x} = (x, y, z)$. These fields can be streamed directly as input from real measurements (see Section 5.2); otherwise, we assume a temperature field that resembles the standard atmospheric

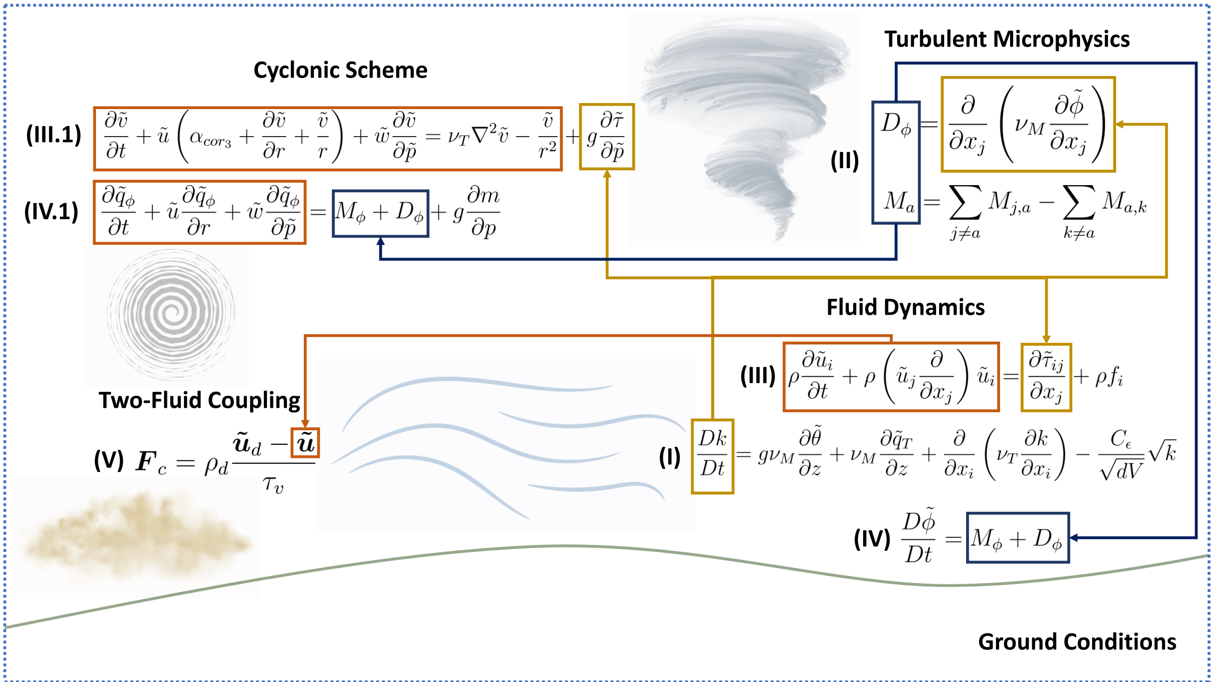

Fig. 3. Schematic representation of our cyclogenesis framework for turbulent heat and water continuity. The arrows indicate different inter-dependencies. Our procedure starts with **(I)** the computation of subgrid kinetic energy; then, we use this result to solve **(II)** the associated turbulent microphysics as well as **(III)** the turbulent fluid dynamics. Afterwards, we use both the velocity field and turbulent terms to compute **(IV)** the transport of atmospheric water content. Note, that our multi-scale scheme uses a different set of equations for steps **(III.1)** and **(IV.1)**, which accounts for different cyclonic phenomena. Finally, for the tornado scheme, we use the computed velocity to solve **(V)** the equations of the coupled dust field.

temperature [ISO 1975], given by

$$T(\boldsymbol{x},t) = \begin{cases} T_G(x,y,t) + \Gamma_0 z\,, & \text{if } 0 \leq z \leq z_1\,, \\ T_G(x,y,t) + \Gamma_0 z_1 + \Gamma_1 (z - z_1)\,, & z_1 \leq z\,, \end{cases} \tag{1}$$

where $T_G(x,y,t)$ is the temperature at ground level, z_1 is the altitude of temperature inversion, and the two lapse rates Γ_0 and Γ_1 control the rate of temperature change. In contrast to Amador Herrera et al. [2021], who considers a completely dry background, we allow initial moisture even before cloud development. This is described by

$$p(\boldsymbol{x},t) = \rho_d R_d T(\boldsymbol{x},t)(1 + 0.61 q_v)\,, \tag{2}$$

where p is the background atmospheric pressure, ρ_d the density of dry air, R_d the gas constant for dry air, and q_v the initial water vapor content in the atmosphere given in terms of its mixing ratio. In terms of non-dimensional pressure Π, this equation can be rewritten as

$$\Pi = \left(\frac{p}{p_G}\right)^{\frac{R_d}{c_p}} = \left(\frac{R_d \rho \theta_v}{p_G}\right)^{\frac{R_d}{c_p}}\,, \tag{3}$$

where p_0 is the pressure at ground level, c_p the heat capacity, and θ_v is the virtual potential temperature [Houze 2014], given by

$$\theta_v = \theta\,(1 + 0.61 q_v)\;,$$

with potential temperature θ defined by $T = \Pi\theta$.

4.1.2 Momentum Equations. The next step in our model consists in describing the turbulent motion of humid air. In particular, we propose a formulation based on the Reynolds-Averaged form of the Navier-Stokes equations (RANS) that can be easily coupled to microphysical phase changes in the atmosphere, e.g., cloud condensation, ice crystallization, etc. In the RANS formulation, it is assumed that the velocity field $\boldsymbol{u}(\boldsymbol{x},t)$ can be decomposed into an average flow velocity $\tilde{\boldsymbol{u}}(\boldsymbol{x},t)$, and a fluctuating term $\boldsymbol{u}^{'}(\boldsymbol{x},t)$, so that

$$\boldsymbol{u}(\boldsymbol{x},t) = \tilde{\boldsymbol{u}}(\boldsymbol{x}) + \boldsymbol{u}^{'}(\boldsymbol{x},t)\,.$$

Other fluid quantities (e.g., pressure, stress, etc.) are decomposed analogously. Then, taking the average value of this system, it is possible to derive a set of correspondent RANS equations describing the average flow of momentum [Alfonsi 2009], given in tensor form

$$\begin{aligned} \rho\frac{\partial \tilde{u}_i}{\partial t} + \rho\left(\tilde{u}_j \frac{\partial}{\partial x_j}\right)\tilde{u}_i &= \frac{\partial \tilde{\tau}_{ij}}{\partial x_j} + \rho f_i\,, \\ \frac{\partial \tilde{u}_i}{\partial x_i} &= 0\,, \end{aligned} \tag{4}$$

where ρ is the density of the fluid, f_i is any external influence, and the total stress tensor $\tilde{\tau}_{ij}$ can be expanded into

$$\tilde{\tau}_{ij} = -\tilde{p}\delta_{ij} + 2\mu\tilde{S}_{ij} - \rho\widetilde{u_i^{'}u_j^{'}}\,,$$

with pressure $\tilde{p}$, dynamic viscosity μ, Reynolds stress tensor $\widetilde{u_i'u_j'}$, and strain rate tensor $\tilde{S}_{ij}$ computed as

$$\tilde{S}_{ij} = \frac{1}{2}\left(\frac{\partial \tilde{u}_i}{\partial x_j} + \frac{\partial \tilde{u}_j}{\partial x_i}\right) .$$

This system of equations can be closed using zero-, one-, and two-moment schemes [Kajishima and Taira 2016]. We propose a one-moment closure model that can also describe microphysical phase changes. First, we assume that vortex tubes evolve without being subject to complex nonlinear interactions, e.g., collisions between tornadoes or with the environment, so we compute the Reynolds stress tensor using the Boussinesq linear eddy-viscosity equation, which reads

$$\widetilde{u_i'u_j'} = -2\nu_T\tilde{S}_{ij} + \frac{2}{3}k\delta_{ij} ,$$

with turbulent viscosity ν_T and turbulent kinetic energy k. Then, we modify the turbulent energy scheme of [Mellor and Yamada 1974] to account for ice-phase transitions, such that the turbulent kinetic energy is given by

$$\frac{Dk}{Dt} = g\nu_M\frac{\partial\tilde{\theta}}{\partial z} + \nu_M\frac{\partial \tilde{q}_T}{\partial z} + \frac{\partial}{\partial x_i}\left(\nu_T\frac{\partial k}{\partial x_i}\right) - \frac{C_\epsilon}{s_k}\sqrt{k^3} , \tag{5}$$

where $D/Dt = \partial/\partial t + \tilde{u}_j\partial/\partial x_j$ is the material derivative, ν_M represents eddy mixing, s_k is the subgrid turbulence scale, $C_\epsilon = 0.2$ is a ventilation coefficient, and, in our specific formulation, $\tilde{q}_T = \tilde{q}_v + \tilde{q}_i + \tilde{q}_c$ is the total mixing ratio of water content in the form of ice, warm cloud, and vapor. The turbulent viscosity and eddy mixing terms are updated as

$$\begin{aligned}\nu_T &= 0.2\, s_k\sqrt{k} , \\ \nu_M &= 3C_e\nu_T ,\end{aligned} \tag{6}$$

where C_e is an eddy coefficient acting as a coupling strength constant between microphysical phenomena and turbulent kinetic energy. Once we have a closed system for turbulent dynamics, we introduce the density-driven buoyancy force via the f_i vector in Eq. (4). Specifically, atmospheric buoyancy is computed following Archimedes' principle, and reads

$$B(\boldsymbol{x}, t) = g\left[\frac{\tilde{\theta}}{\tilde{\theta}_0} - 1 + 0.61\tilde{q}_v - \sum_a \tilde{q}_a\right] . \tag{7}$$

Finally, the Coriolis effect is incorporated directly by an additional term $R_{\mathrm{cor}\,i} = \epsilon_{ijk}\boldsymbol{\alpha}_{\mathrm{cor}\,j}\tilde{u}_k$, where $\boldsymbol{\alpha}_{\mathrm{cor}}$ is a vector representing the angular velocity with respect to each coordinate axis.

4.1.3 Turbulent Microphysics. The formation of different cloud configurations in the atmosphere is heavily influenced by microphysical processes [Amador Herrera et al. 2021]. Since we want to model not only the turbulent flow of wind, but also the formation, maturation, and dissipation of cloud cyclone structures, we incorporate a microphysics scheme that can describe water phase changes under turbulent motion. Our microphysics model, illustrated schematically in Figure 4, consists of an extra system of coupled transport equations that account for the diverse physical interactions between different hydrometeors. In general, the microphysics parametrization $M_{a,b}(T, p, q_a, q_b)$ of a species a transitioning into b (e.g., snow melting into rain $M_{s,r}$) will be a function of local temperature, pressure, and current mass fractions of a and b. The total rate of phase change of a hydrometeor a is then expressed as

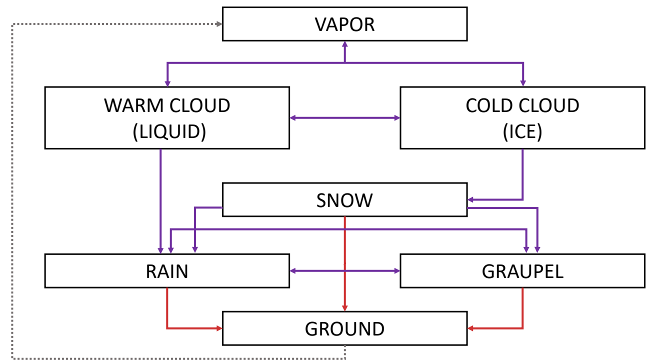

Fig. 4. Illustration of the turbulent microphysics model for the transport between different cloud and precipitation types. The scheme includes both microphysical matter transport M_ϕ as well as turbulence mixing D_ϕ per phase transition.

$$M_a = \sum_{j\neq a} M_{j,a} - \sum_{k\neq a} M_{a,k} , \tag{8}$$

where the sources $M_{j,a}$ and sinks $M_{a,k}$ include transitions via condensation, deposition, sublimation, evaporation, etc. The explicit parametrization of each process is taken directly from Amador Herrera et al. [2021]. We further modify this equation to include additional eddy mixing of temperature and hydrometeors. Then, our general expression for the dynamics of potential temperature $\tilde{\theta}$ and mixing ratios $\tilde{q}_a$ is given by

$$\frac{D\tilde{\phi}}{Dt} = M_\phi + D_\phi , \tag{9}$$

where ϕ represents a temperature or mixing ratio field, M_ϕ is the usual microphysical term, and D_ϕ is a turbulence mixing variable. In particular, M_θ represents the local change in temperature due to water phase transitions, so it is given by

$$M_\theta = \sum_t \frac{L_t}{c_p} X_a , \tag{10}$$

where the sum runs over all phase transitions, L_t is the latent heat of the transition, and X_a the mass fraction of each hydrometeor. From mixing length theory, it is known that the turbulent mixing of fields acts as an enhanced diffusion process scaled by the turbulent kinetic energy. For this reason, we use the prognosis equations

$$D_\phi = \frac{\partial}{\partial x_j}\left(\nu_M\frac{\partial\tilde{\phi}}{\partial x_j}\right) , \tag{11}$$

where the eddy mixing term ν_M explicitly models the influence of turbulent kinetic energy on enhanced microphysical diffusion.

4.1.4 Vorticity Dynamics. In vector form, the first expression in Eq. (4) can be written as

$$\frac{\partial\tilde{\boldsymbol{u}}}{\partial t} + (\tilde{\boldsymbol{u}}\cdot\nabla)\,\tilde{\boldsymbol{u}} = \frac{1}{\rho}B\hat{\boldsymbol{k}} + \boldsymbol{F} + \frac{2\mu}{\rho}\nabla^2\tilde{\boldsymbol{u}} - \nabla\tilde{p} ,$$

where we have grouped the turbulent and Coriolis terms in

$$\boldsymbol{F} = 2\nu_T \rho \nabla^2 \tilde{\boldsymbol{u}} - \frac{2}{3}\nabla k + \boldsymbol{\alpha}_{\mathrm{cor}} \times \tilde{\boldsymbol{u}}\,.$$

Computing the curl on both sides of Eq. (4.1.4), we get the dynamic equations for turbulent vorticity $\tilde{\boldsymbol{\omega}} = (\nabla \times \tilde{\boldsymbol{u}})$, written as

$$\begin{aligned} \frac{D\tilde{\omega}_z}{Dt} &= \tilde{\boldsymbol{\omega}}_h \cdot \nabla_h \tilde{u}_z + \tilde{\omega}_z \frac{\partial \tilde{u}_z}{\partial z} + \boldsymbol{F}_z^{'}\,, \\ \frac{D\tilde{\boldsymbol{\omega}}_h}{Dt} &= \tilde{\boldsymbol{\omega}} \cdot \nabla \boldsymbol{u}_h + \nabla \times \left(B\hat{\boldsymbol{k}}\right) + \boldsymbol{F}_h^{'}\,, \end{aligned} \tag{12}$$

where the subscripts z and h indicate the vertical and horizontal components of a vector, respectively, and $\boldsymbol{F}^{'} = \nabla \times \boldsymbol{F}$ is the curl of all fields included in $\boldsymbol{F}$. We see from the right-hand-side of Eq. (12) that, for a velocity field that starts with no prescribed rotation, the process of cyclogenesis is started by the tilting $\boldsymbol{\omega} \cdot \nabla \boldsymbol{v}_h$ and mixing $\boldsymbol{F}_z^{'}$ parameters, which transform horizontal vortex lines into the vertical vortex tubes that form a tornado. The production of vertical vorticity, then, depends crucially on both turbulence mixing fields and environmental wind-shear.

4.2 Two-Fluid Tornadic Parametrization

The process of tornadogenesis involves the development of several vortex tubes in the wind field, even at zones where condensation is not present. These tubes can be visualized and analyzed directly by plotting $\boldsymbol{\omega}$ [Orf 2019]. However, this approach does not capture the expected visuals of a tornado made of dust and debris that got inside the non-condensed vortexes. Instead, we use an approach close to the Two-Fluid Model (TFM) of Liu et al. [2006], in which a dust field is coupled to $\tilde{\boldsymbol{u}}$ to enhance tornado visualization by incorporating the movement of debris particles. Note, however, that in TFM only the bottom tornadic region is considered, i.e., there is no mesoscale or cloud simulation. Since the dust field $\tilde{\boldsymbol{u}}_{\mathrm{dust}}$ does not involve any microphysical change, but constant particles of radius r_{dust}, we propose a zero-moment RANS, which reads

$$\begin{aligned} \rho_{\mathrm{dust}} \frac{D\tilde{\boldsymbol{u}}_{\mathrm{dust}}}{Dt} &= \nu_{\mathrm{dust}} \nabla^2 \tilde{\boldsymbol{u}}_{\mathrm{dust}} - \nabla \tilde{p}_{\mathrm{dust}} \\ &\quad + \nabla \cdot \tilde{\boldsymbol{\tau}}_{\mathrm{dust}} + \boldsymbol{F}_{\mathrm{dust}} + m_{\mathrm{dust}} \boldsymbol{g}\,, \\ \nabla \cdot \tilde{\boldsymbol{u}}_{\mathrm{dust}} &= 0\,, \end{aligned} \tag{13}$$

with debris mass m_{dust}, viscosity ν_{dust}, zero-moment Reynolds stress $\tilde{\boldsymbol{\tau}}_{\mathrm{dust}}$, pressure p_{dust}, density ρ_{dust}, gravitational constant $\boldsymbol{g}$, and external forces $\boldsymbol{F}_{\mathrm{dust}}$. In particular, $\boldsymbol{F}_{\mathrm{dust}}$ contains the coupling term $\boldsymbol{F_c}$ between air and dust. The interaction is parametrized as

$$\boldsymbol{F}_c = \rho_{\mathrm{dust}} \frac{\tilde{\boldsymbol{u}}_{\mathrm{dust}} - \tilde{\boldsymbol{u}}}{C_{\mathrm{dust}}}\,, \tag{14}$$

where the scalar C_{dust} is computed as

$$\begin{aligned} C_{\mathrm{dust}} &= \frac{m_{\mathrm{dust}}}{3\pi r_{\mathrm{dust}} \nu_{\mathrm{dust}}} \left(1 + \frac{\mathrm{Re}}{60} + \frac{\mathrm{Re}/4}{1+\sqrt{\mathrm{Re}}}\right), \\ \mathrm{Re} &= \rho_{\mathrm{dust}} r_{\mathrm{dust}} \|\nabla^2 \tilde{\boldsymbol{u}}\| / \nu_{\mathrm{dust}}\,. \end{aligned}$$

Finally, the zero-moment Reynolds stress is computed as

$$\tilde{\boldsymbol{\tau}}_{\mathrm{dust}} = \rho_{\mathrm{dust}} \left\| \frac{\partial \tilde{\boldsymbol{u}}_d}{\partial z} \right\| \frac{z^2}{c_k^2}\,,$$

where z is the altitude, and $c_k = 0.4$ is the Von Kármán constant.

4.3 Cyclone Scheme

As opposed to tornadic phenomena, the primary energy source for the genesis and maintenance of tropical cyclones is the latent heat released by condensation of oceanic water [Holland and Merrill 1984]. In this sense, the large-scale motion in a hurricane consists of an axis-symmetric forced circulation driven by the heat released in convective cells. Based on this, we propose a numerical model for the treatment of mesoscale cyclonic dynamics based on the assumptions of axial symmetry and hydrostatic balance, similar to planetary boundary layer (PBL) approaches [Moeng 1984]. In cylindrical coordinates (r, γ, z), we express the velocity using its radial, tangential, and vertical components ($\tilde{\boldsymbol{u}}_{\mathrm{rad}}$, $\tilde{\boldsymbol{u}}_{\mathrm{tan}}$, and $\tilde{\boldsymbol{u}}_{\mathrm{vert}}$, respectively), so that the RANS equations for a meridional plane are given by

$$\begin{aligned} \frac{\partial \tilde{\boldsymbol{u}}_{\mathrm{tan}}}{\partial t} + \tilde{\boldsymbol{u}}_{\mathrm{rad}} \left(\alpha_{\mathrm{cor}_3} + \frac{\partial \tilde{\boldsymbol{u}}_{\mathrm{tan}}}{\partial r} + \frac{\tilde{\boldsymbol{u}}_{\mathrm{tan}}}{r}\right) + \tilde{\boldsymbol{u}}_{\mathrm{vert}} \frac{\partial \tilde{\boldsymbol{u}}_{\mathrm{tan}}}{\partial \tilde{p}} &= \\ = \nu_T \nabla^2 \tilde{\boldsymbol{u}}_{\mathrm{tan}} - \frac{\tilde{\boldsymbol{u}}_{\mathrm{tan}}}{r^2} + g \frac{\partial \tilde{\tau}}{\partial \tilde{p}}\,&, \\ \tilde{\boldsymbol{u}}_{\mathrm{tan}} \left(\alpha_{\mathrm{cor}_3} + \frac{\tilde{\boldsymbol{u}}_{\mathrm{tan}}}{r}\right) = \frac{\partial \Phi}{\partial r}\,&, \end{aligned} \tag{15}$$

where Φ the geopotential associated to the earth's gravitational field. Additionally, the conservation of energy in cylindrical coordinates is expressed as

$$\frac{\partial \tilde{\theta}}{\partial t} + \tilde{\boldsymbol{u}}_{\mathrm{rad}} \frac{\partial \tilde{\theta}}{\partial r} + \tilde{\boldsymbol{u}}_{\mathrm{vert}} \frac{\partial \tilde{\theta}}{\partial \tilde{p}} = \frac{Q}{\tilde{\Pi} c_p} + \nu_T \nabla^2 \tilde{\theta} + \frac{g}{\tilde{\Pi} c_p} \frac{\partial h}{\partial \tilde{p}}\,, \tag{16}$$

where h is the vertical flux of sensible heat, and Q measures non-adiabatic heating per unit mass and unit time. Moreover, the hydrostatic relation for the geopotential reads

$$\frac{\partial \Phi}{\partial \tilde{p}} = -\frac{R_d \tilde{\Pi}}{\tilde{p}} \tilde{\theta}\,. \tag{17}$$

Finally, the mixing ratio relations are written as

$$\frac{\partial \tilde{q}_\phi}{\partial t} + \tilde{\boldsymbol{u}}_{\mathrm{rad}} \frac{\partial \tilde{q}_\phi}{\partial r} + \tilde{\boldsymbol{u}}_{\mathrm{vert}} \frac{\partial \tilde{q}_\phi}{\partial \tilde{p}} = M_\phi + D_\phi + g \frac{\partial m}{\partial \tilde{p}}\,, \tag{18}$$

where m represents the vertical flux of moisture. We describe the mean stress tensor, as well as the fluxes of momentum, sensible heat, and moisture using the usual prognosis equations for tropical cyclones [Kepert 2010], given by

$$\begin{aligned} \tilde{\tau} &= \rho_d \|\tilde{\boldsymbol{u}}\| \tilde{\boldsymbol{u}}_{\mathrm{tan}}\,, \\ h &= c_p \rho_d \|\tilde{\boldsymbol{u}}\| T\,, \\ m &= \rho_d \|\tilde{\boldsymbol{u}}\| q_v\,, \\ Q &= c_p \left(\tilde{\Pi}\tilde{\theta} - T\right)\,. \end{aligned} \tag{19}$$

Finally, to evaluate the derivatives with respect to pressure, we use the chain rule and the radial pressure gradient

$$\frac{\partial \tilde{p}}{\partial r} = \frac{B}{r} \left(\frac{R_{\max}}{r}\right)^B \exp\left[-\left(\frac{R_{\max}}{r}\right)^B\right],$$

where $B = 0.5$ is Holland's radial pressure profile parameter [1980], and $R_{\max}$ is the maximum radius variable (with approximative values of 8 km for small storms, and up to 150 km for large hurricanes).

ALGORITHM 1: Cyclogenesis Algorithm.

Input: Current system state ($\tilde{\boldsymbol{u}}$, $\tilde{\boldsymbol{u}}_d$, k, $\tilde{\theta}$, $\tilde{q}_a$).
Output: Updated system state.
Procedure:
$T, p \longleftarrow$ Update background temperature and pressure using either input data or Eqs. (1) and (2).
$k \longleftarrow$ Advect and diffuse turbulent energy k.
$\nu_T \longleftarrow 0.2 s_k \sqrt{k}$ Update turbulent viscosity
$\nu_M \longleftarrow 3C_e \nu_T$ Update eddy mixing
$X_a \longleftarrow \tilde{q}_a/\tilde{q}_a{+}1$ Convert mixing ratio to mass fraction
$B \longleftarrow$ Compute buoyancy force according to Eq. (7).
$\boldsymbol{F_c} \longleftarrow$ Update wind-debris interaction term following Eq. (14)
$\boldsymbol{w} \longleftarrow$ Advect vorticity as an independent field, according to Eq. (12).
$\tilde{\boldsymbol{u}} \longleftarrow \tilde{\boldsymbol{u}} + \boldsymbol{B} + \Delta x \boldsymbol{N} \times \boldsymbol{w}$ Apply buoyancy and vorticity confinement
$\tilde{\boldsymbol{u}} \longleftarrow$ Advect, diffuse, and pressure project the wind field
$\tilde{\boldsymbol{u}}_d \longleftarrow$ Advect, diffuse, and pressure project debris field
$M_\theta \longleftarrow \sum_t L_t X_a / c_p$ Compute temperature change
$\tilde{\phi} \longleftarrow \tilde{\phi} + M_\phi + D_\phi$ Turbulent Microphysics
$\tilde{\phi} \longleftarrow$ Advect and diffuse additional fields
end

ALGORITHM 2: Mesoscale Cyclone Algorithm.

Input: Current system state ($\tilde{\boldsymbol{u}}$, $\tilde{\boldsymbol{u}}_d$, k, $\tilde{\theta}$, $\tilde{q}_a$).
Output: Updated system state.
Procedure:
$T, p \longleftarrow$ Update background temperature and pressure using either input data or Eqs. (1) and (2).
$k \longleftarrow$ Advect and diffuse turbulent energy k.
$\nu_T \longleftarrow 0.2 s_k \sqrt{k}$ Update turbulent viscosity
$\nu_M \longleftarrow 3C_e \nu_T$ Update eddy mixing
$\tilde{\tau}, h, m, Q \longleftarrow$ Update moisture, momentum, and sensible heat fluxes using Eq (19).
$X_a \longleftarrow \tilde{q}_a/\tilde{q}_a{+}1$ Convert mixing ratio to mass fraction
$B \longleftarrow$ Compute buoyancy force according to Eq. (7).
$\boldsymbol{w} \longleftarrow$ Advect vorticity as an independent field, according to Eq. (12).
$\tilde{\boldsymbol{u}} \longleftarrow \tilde{\boldsymbol{u}} + \boldsymbol{B} + \Delta x \boldsymbol{N} \times \boldsymbol{w}$ Apply buoyancy and vorticity confinement
$\tilde{\boldsymbol{u}} \longleftarrow$ Advect and diffuse the wind field following Eq. 15
$\tilde{\theta} \longleftarrow$ Advect and diffuse potential temperature following Eq. (16)
$\tilde{\phi} \longleftarrow \tilde{\phi} + M_\phi + D_\phi$ Turbulent Microphysics
$\tilde{\phi} \longleftarrow$ Advect and diffuse additional fields according to Eq. (18)
end

5 ALGORITHMICS

In the following, we provide details for the numerical integration procedure, including the setup of our discretization scheme, boundary conditions, and solver. Our tornadic and cyclone frameworks are summarized in Algorithm 1 and Algorithm 2, respectively.

5.1 Numerical Integration

The turbulent heat, water, and fluid dynamic models described in the previous section provide the basis for the implementation of our cyclone simulation framework.

5.1.1 Mesh Structure. We set up a staggered 3D voxel space using an uniform grid scale Δx, and set $s_k = (\Delta x \Delta y \Delta z)^{1/3} = \Delta x$. We store the current state of our atmospheric system in this grid: velocity fields $\tilde{\boldsymbol{u}}$ and $\tilde{\boldsymbol{u}}_{\text{dust}}$ are stored at the faces, while turbulent kinetic energy k, mixing ratios q_a, potential temperature $\tilde{\theta}$, and vorticity $\tilde{\boldsymbol{\omega}}$ are stored at the center. Additionally, we discretize all the derivative operators using centered finite differences, as shown in Appendix A.4. To account for ground conditions, e.g., temperature, water content, and pressure, we also include a 2D uniform grid using the same scale Δx, as well as a height map $\mathcal{H} : (x_1, x_2) \rightarrow \mathcal{H}(x_1, x_2)$ such that the ground mesh is embedded in the 3D space as $\partial\Omega_{\text{bottom}} = (x_1, x_2, \mathcal{H}(x_1, x_2)) \in \Omega$. To update the terms involving material derivatives, we use a semi-Lagrangian scheme, while quantities that are updated directly, e.g., mixing coefficients and atmospheric profiles, are computed on the fly.

5.1.2 Implementation. First, the subgrid kinetic energy k is advected while no-slip conditions are set at the bottom, and free-slip boundaries at the ceiling and walls. After updating the eddy coefficients, heat transfer and microphysical terms, we compute the relevant fields that control the forces acting on the velocity field (e.g., buoyancy for tornadic phenomena and also sensible heat fluxes in the case of mesoscale cyclones). Then, the wind field is advected followed by the integration of viscosity-related effects by solving the corresponding diffusion process [Stam 1999]. For the advection process, we employ the same boundary conditions as those for subgrid kinetic energy. Finally, when updating the potential temperature and hydrometeor particles through their material derivatives, we set $\tilde{\theta}$ to the ambient temperature at the boundary; additionally, periodic boundary conditions are used for vapor $\tilde{q}_v$, and all the other hydrometeors $\tilde{q}_\phi$ are set identically to zero at the sides. For our hurricane scheme, we set $\tilde{v}$ to zero at the origin $r = 0$, as well as $\partial\tilde{\theta}/\partial r = \partial\tilde{q}_\phi/\partial r = 0$. The surrounding $r_{\max}$ conditions are set the same as in rectangular coordinates. Finally, for the debris field $\tilde{\boldsymbol{u}}_d$ we set Dirichlet boundaries at the bottom (the amount of dust in the ground), periodic conditions at the sides, and free-slip at the top.

5.1.3 Vorticity Confinement. We implement vorticity confinement to mitigate the effects of numerical dissipation. However, we found that by updating the vorticity for the confinement process using Eq. (12) instead of the usual numerical cross product, the quantitative results of angular velocity for hurricanes were closer to real measurements (Figures 23 and 24) without requiring fine-tuning. Specifically, we treat the vorticity as an additional field that is added to the wind velocity via confinement with a force $\boldsymbol{f_w} = \Delta x \boldsymbol{N} \times \boldsymbol{w}$, where $\boldsymbol{N} = \nabla\eta/|\nabla\eta|$ and $\eta = |\boldsymbol{w}|$. Note that, since we only use the vorticity to reduce numerical dissipation and not to reconstruct the velocity field, the momentum equation is only advected one time, and we do not need to solve additional stream functions.

5.1.4 Numerical Solver. In both of our cyclone generation schemes, we use a one-moment turbulence approach based on computing the contribution of subgrid turbulent energy to the average turbulent atmospheric flow. Additionally, our microphysics scheme also computes averaged quantities over ensembles of particles that would be otherwise resolved at a subgrid scale. Given this multi-scale nature of our framework, a natural path to solve our RANS formulation in a highly efficient manner is to use a state-of-the-art algebraic multigrid (AMG) solver, Specifically, we use the AMGCL solver proposed by Demidov [2019], which is able to efficiently solve large sparse linear systems.

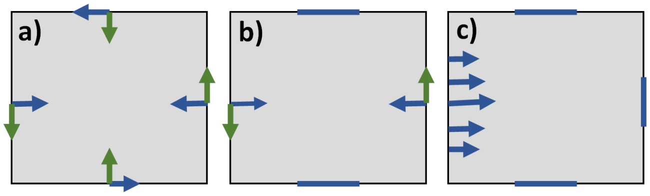

Fig. 5. Schematic representation of possible boundary conditions for the velocity field. Previous schemes for the visual simulation of tornadoes depend heavily on *a priori* rotation conditions (a). In contrast, our physically based model can produce vortex motion even when rotation is not prescribed at the boundary (b) and also with dynamic conditions like inlet gravity waves (c).

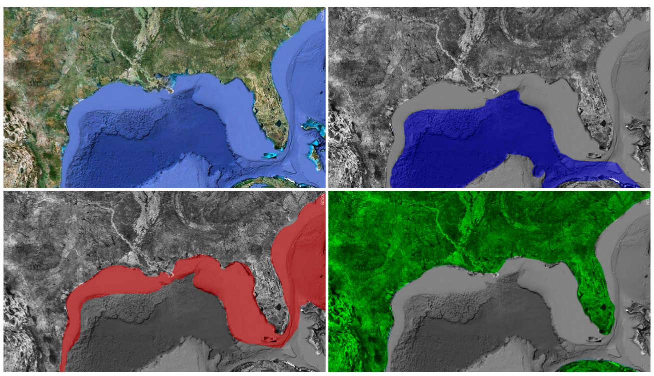

Fig. 6. We incorporate oceanic water masses into our framework by coding different zones in the mesh via material maps using satellite data of the region of interest. These images are, from left to right, top to bottom: The satellite image, water content map, surface temperature map, and heat capacity map.

5.2 Dynamic Boundary Conditions

In general, cyclonic schemes for the efficient visual simulation of tornadic phenomena heavily rely on the boundary conditions of $\tilde{\boldsymbol{u}}$ for the generation of vorticity. In consequence, it is customary in these methods to adopt fixed no-slip and Dirichlet boundaries at the sides, top and bottom of the mesh to generate an *a priori* rotational field [Ding 2005]. This approach has been useful to simulate different tornadic phenomena, e.g., the simulation of destructive tornadoes by Liu et al. [2007], but it restricts both the domains and cyclonic effects that can be modeled. In contrast, our physically inspired model can produce vorticity even when rotation is not prescribed at the boundary. As shown in Figure 5, we use two types of boundaries at the lateral walls of the domain: Incoming wind shear $\boldsymbol{W} = (U, V, 0)$ from two opposite sides, which fuels a sustained turbulent flow, and dynamic boundaries, like inlet gravity waves. We parametrize inlet conditions using a periodic wave form

$$\tilde{\boldsymbol{u}}_h = W \exp\left[i\left(k_1 x + l_1 y - \omega_1 t\right)\right], \tag{20}$$

where the wave-numbers k_1, l_1, ω_1 are fixed parameters that determine the specific form of the impulse. Then, we take the real part of this inlet wave into the boundary condition. For hurricane simulations, the distribution of humidity $\tilde{q}_\phi$ at ground level determines

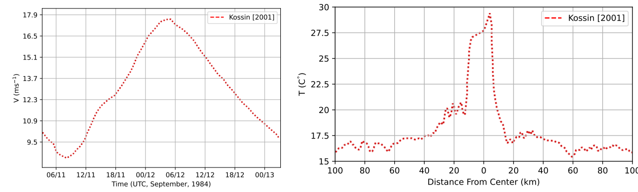

Fig. 7. We enable dynamic boundaries by streaming real-data measurements of cyclone events. For instance, (left) the velocity at the $r = 5$ km boundary from the center of the cyclone is used for simulations of the hurricane eye, while (right) temperature profiles are streamed as ground boundaries (by fixing $T_G(x, y) = T_{\text{profile}} - \Gamma z_{\text{profile}}$) for simulating the whole cyclone structure. Additional time-dependent profiles for humidity and pressure can be streamed into our framework analogously. These plots are reproduced using data from Kossin and Eastin [2001].

the regions where vorticity is further enhanced via flux of heat. The pivotal role of latent heat release for hurricane development has been verified before both numerically [Drennan et al. 2007] and experimentally [Rodgers et al. 1998]. We incorporate this into our model by prescribing oceanic water content by color-coding different zones in the domain with material maps, as shown in Figure 6. We use four maps to encode, respectively, surface temperature T_G, humidity q_v, heat capacity c_p, and the presence of *oceanic water*.
The development and subsequent decay of cyclonic phenomena depend not only on the local turbulent transport of heat and water, but also on global weather conditions, which we incorporate as the boundary values of incoming winds, temperature, pressure, and humidity in the environment. To simulate global changes in the environment surrounding the cyclone, we enable the dynamical change of our boundary conditions. For incoming winds, the time-dependence is directly encoded in $\boldsymbol{W} = \boldsymbol{W}(t)$, e.g., for periodic wave forms as discussed before, or simply by reducing the wind shear intensity over time. Additionally, we use dynamic boundary values when streaming real-data measurements into our framework. For instance, for the simulation of specific hurricane events like Katrina and Diane, we directly stream as boundary conditions real measurements of temperature, pressure, and surrounding wind shear profiles that were taken during the evolution of those cyclones. This is illustrated in Figure 7.

6 RESULTS

In this section, we present a variety of results simulated with our C++/CUDA framework implemented as described in the previous section. Table 1 provides an overview of the different scenes presented throughout this section, including relevant parameters. Computation times listed in Table 1 are measured using an NVIDIA®GTX 2080 Ti, with double precision floating point arithmetic.

6.1 Vortex Generation

First, we validate the different components of our *cyclogenesis* framework by comparing the generation of vortex phenomena with different approaches.

Table 1. Overview of the relevant parameters used in the scenes presented in this paper. For all scenes, a constant time step size of $\Delta t = 5$ min is used. Parameters are listed in $[T_G] = 1°\mathrm{C}$, $[\overline{q}_{gr}] = 1\,\mathrm{kg\ kg}^{-1}$, and $[W] = 1\,\mathrm{km\,hr}^{-1}$. Identical parameter values $\rho_d = 2500\,\mathrm{kg\,m}^{-3}$, $c_k = 0.4$, $\Gamma = -6.5$ K/km, and $z_1 = 8$ km are used in all simulations. Resolution (**R**) and runtime (**T**) in seconds per frame are listed.

Fig.	**Scene**	T_G	$\overline{q}_{gr}$	W	C_e	**R**	**T**
1	Hurricane	19	0.90	150	0.8	$800 \times 64 \times 800$	0.15
8	Vortex Generation	22	0.80	30	0.4	$512 \times 128 \times 512$	0.11
9	Turbulence Comparison	22	0.80	30	0.4	$512 \times 128 \times 512$	0.11
10	RANS Comparison	22	0.80	30	0.4	$512 \times 128 \times 512$	0.11
11	Tornado Comparison	22	0.85	30	0.4	$512 \times 128 \times 512$	0.12
12	Hurricane Comparison	19	0.95	180	0.7	$512 \times 128 \times 512$	0.13
14	Parameter Space	21	0.80	–	–	$512 \times 128 \times 512$	0.11
15	*Rope* Tornado	21	0.82	30	0.4	$512 \times 128 \times 512$	0.11
15	*Funnel* Tornado	21	0.84	150	0.4	$512 \times 128 \times 512$	0.11
15	*Wedge* Tornado	26	0.82	300	0.6	$512 \times 128 \times 512$	0.13
15	*Bowl-Shape* Tornado	18	0.86	200	0.5	$512 \times 128 \times 512$	0.12
15	*Landspout*	17	0.75	50	0.5	$512 \times 128 \times 512$	0.11
15	*Multi-Vortex* Tornado	15	0.89	250	0.8	$512 \times 128 \times 512$	0.14
17	Dust Devil	22	0.20	150	0.5	$512 \times 128 \times 512$	0.11
21	Tornadogenesis	18	0.81	200	0.6	$512 \times 128 \times 512$	0.13
22	Tornado Transition	18	0.81	200	0.6	$512 \times 128 \times 512$	0.14
19	Hurricane Eye	19	0.90	150	0.8	$800 \times 64 \times 800$	0.16

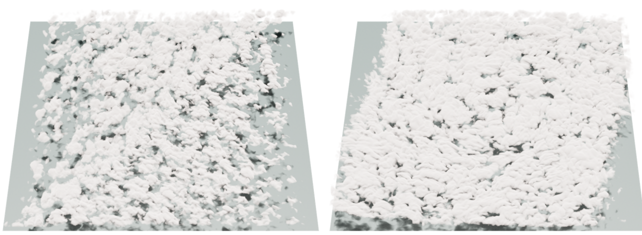

Fig. 8. Simulation using non-rotational wind shear at the walls, corresponding to Figure 5 (b), using the *weatherscapes* model (left) and our framework (right). The emergent vortex formation is only possible in our extended model.

6.1.1 Turbulent Microphysics. As demonstrated in Figure 8, the *weatherscapes* framework of Amador Herrera et al. [2021] is not able to generate vortexes unless explicit rotational boundaries are specified. Moreover, even with prescribed rotation, the tornado generated by *weatherscapes* is less visually appealing because it lacks subgrid details caused by both tilting and turbulence effects, as shown in Figure 10. These experiments show the advantages of explicitly modeling turbulent microphysics phenomena for simulating cyclonic motion in the atmosphere.

6.1.2 One-Moment RANS. Previous tornadic schemes [Ding 2005; Liu et al. 2007] are able to capture interesting vortex dynamics of tornadoes using a zero-moment RANS formulation for turbulent dynamics. However, these schemes model only the lower part of the tornadic region, and do not take into account the associated rotating supercell. In Figure 10, we show the simulation of a rotating cluster of clouds using a zero-moment closure and our model. The inclusion of turbulent microphysics enables us to formulate a one-moment closure system which, in turn, eliminates the artifacts at the boundaries of the cluster.

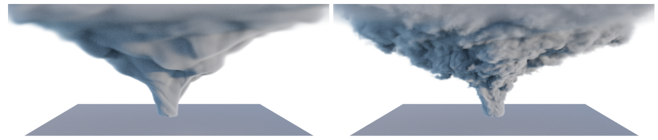

Fig. 9. Simulation of a tornado formed by fully rotational boundary conditions using the *weatherscapes* model (left) and our framework (right). In their model, there is no tilting of vorticity nor turbulence modeling. Hence, there is no generation of vertical vorticity, which is necessary to resolve additional structural details of the tornado.

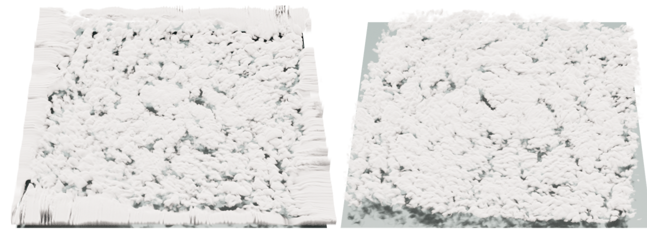

Fig. 10. When simulating the rotation of both supercell and its associated tornado, considering a zero-equation approach for RANS generates artifacts at the boundaries (left), while our one-equation model closed with turbulent microphysics consistently handles rotational supercells (right).

6.1.3 Force-Driven Approach. Outside of weather phenomena, many efforts have been made to incorporate turbulent dynamics into visual simulations. In particular, the MacCormack scheme [Selle et al. 2008] is close to our framework as it is built on top of the usual semi-Lagrangian solver for smoke motion while incorporating a second-moment closure for turbulence. In Figure 11, we compare the simulation of a tornado with our framework and a force-driven approach using the MacCormack scheme. In order to ensure a fair comparison, we use the same boundary conditions at the sides and top of the domain, while the bottom boundary in the force-driven case is set to a vertical shear $W\hat{\boldsymbol{k}}$ around the inlet to simulate the buoyancy in the atmosphere.

While the force-driven simulation is able to produce interesting subgrid turbulence, as in Liu et al. [2007], it does not capture the global shape of the tornado, including the parent supercell, because the formation of these atmospheric structures is governed not only by wind motion but also by phase transitions at the microphysical level (e.g., different cloud types vary in their particle compositions [Amador Herrera et al. 2021]). Moreover, the process of cyclogenesis is not reproduced correctly by the force-driven approach because it generates the vortex from bottom to top following the wind field. In contrast, the tornado in our model grows from top to bottom, following the direction of condensation, even though the wind field is moving upwards. Analogously, the force-driven approach can be used to simulate a mesoscale vortex but, as demonstrated in Figure 12, it is not able to reproduce the *eye* structure of a hurricane.

In Figure 13, we show quantitative measurements of these experiments. In summary, we observe that a turbulent force-driven model can simulate wind fields similar to those encountered in atmospheric cyclones but the lack of microphysical phase transitions impacts

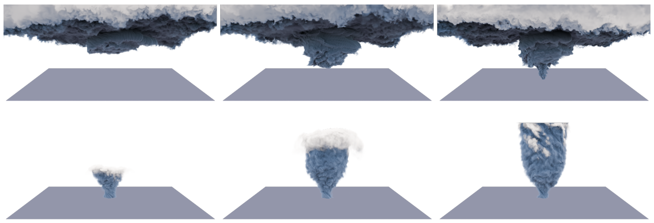

Fig. 11. Time evolution (from left to right) of a tornado simulated using our framework (top) and a force-driven approach (bottom). Since it does not model the different microphysical phase transitions in the atmosphere, the force-driven scheme is not able to reproduce the process of cyclogenesis nor the global tornadic structure, including the parent supercell.

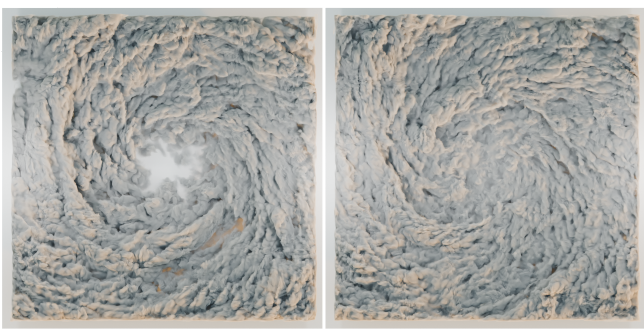

Fig. 12. Hurricane simulated using our framework (left) and a turbulent force-driven approach (right). The lack of microphysical modelling in the force-driven approach forms a hurricane without an *eye* region, where the atmospheric temperature and pressure stops cloud condensation.

the final global geometry of the vortex (Figure 12) and the vertical cloud fraction profiles (Figure 13).

6.2 Vortex Control

Our physically based model enables us to easily control the simulation of vortex dynamics via a lightweight canonical parameter set. In particular, while the temperature and water content determine the final cloud geometry, the number and strength of vortex tubes can be easily controlled via the turbulence or mixing coupling constant C_e, and the boundary wind shear magnitude $||\boldsymbol{W}||$. More intense winds generate greater angular velocities, while higher values of the turbulence constant increase the number of vortexes.

6.3 Tornado Types

As demonstrated in Figure 15, our framework is able to simulate different types of tornadoes caused by the complex interplay of a turbulent atmosphere, microphysical phenomena, and wind shears: (a) Using low eddy mixing coefficients C_e as well as low shear $||\boldsymbol{W}||$ forms relatively uniform and dense cold clouds that trigger small vortex tubes beneath them. Some of these tubes carry the necessary pressure and temperature conditions to generate condensation along their path, which in turn creates small *rope* tornadoes. (b, c) Increasing the shear while maintaining relatively low mixing

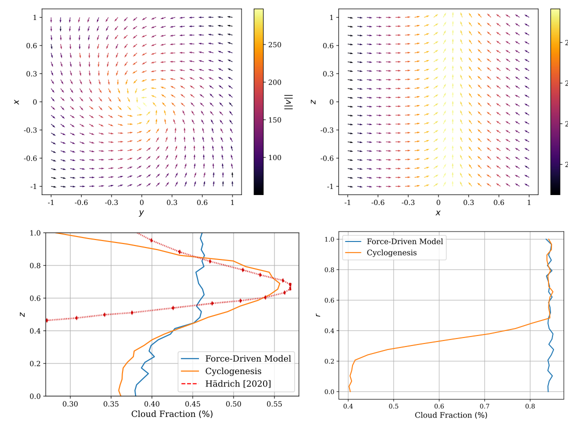

Fig. 13. Different measurements from the simulations presented in Figures 11 and 12. The force-driven scheme is able to reproduce wind fields similar to those encountered in an atmospheric cyclone (top, cross sections yz and xz of the wind field in normalized coordinates). However, it does not capture the amount of cloud matter (i.e., the average cloud fraction in the z-axis) in the atmosphere, which depends also on microphysical phase changes. This is the case for both tornadic (bottom-left) nor hurricane (bottom-right) phenomena. The plot of cloud fraction for the tornado includes a reproduction of the supercell simulation (without tornado) of Hädrich et al. [2020] for comparison.

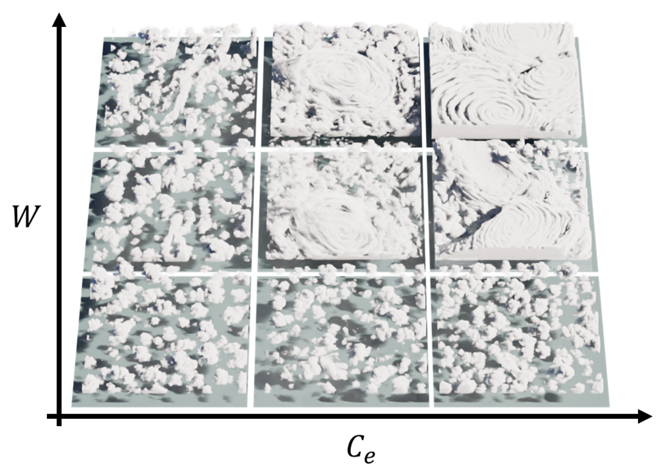

Fig. 14. Parameter space exploration varying the eddy mixing coefficient C_e and wind shear $||\boldsymbol{W}||$. Atmospheric parameters are identically set to $T_G = 21°C$, and $q_v = 0.8$. Stronger winds and greater eddy coefficients result in more vortex tubes and greater vorticity in general.

coefficients introduce enough turbulence into the system to sustain a greater vortex tube of condensation and debris that is captured from the ground, forming a *cone* or *funnel* tornado. (d, e) When we further increase C_e, the vorticity field generates multiple small vertical vortex tubes that are combined into a single large eddy of condensation and precipitation around it in the form of rain. These wider eddies are called *wedge* tornadoes, and are usually within the EF4-EF5 category on the Enhanced Fujita scale. (f) Decreasing the temperature while increasing the amount of humidity q_v in the atmosphere enables us to simulate the base of mixed-phase cumulonimbus clouds where vorticity is present at the rotating base but pressure and temperature conditions do not allow condensation at such altitudes, which results in a *bowl-shaped* tornado. (g) Increasing the mixing coefficients in this conditions enables some vorticity tubes to travel down the atmosphere even when they transport no condensation. When such a tube reaches the ground, it may trap debris around it, which allows to visualize part of the vortex connecting the ground and the base of the cloud. This phenomena is commonly known as *landspout.* (h) Increasing both wind-shear and eddy mixing enables us to simulate strong turbulence dynamics that can sustain *multiple-vortex* tornadoes at the base of the cumulonimbus.

An additional benefit of a physically-based model over turbulent force-driven schemes is that we can compute the value of diverse atmospheric quantities and compare against real data. For instance, in Figure 16 we show the correlation between the Bulk Richardson Number (BRi) – a ratio of buoyancy to vertical shear – and the Storm Relative Enviromental Helicity (SREH) – a measure of the streamwise vorticity within the inflow environment of a convective storm – with the intensity of a tornado in the Enhanced Fujita scale, and how our computations compare with the data measured by Colquhoun and Riley [1996] and later extended by Anderson-Frey et al. [2019]. For the comparisons, we simulated thirty funnel tornado events per Enhanced Fujita category, while varying the velocities within the velocity range of real events. Our simulation results match the observed correlations in real tornadoes. The computations of BRi and SREH are detailed in Appendix A.3.

6.4 *Dust Devils*

Similar to *landspouts*, *dust devils* are ground-based whirlwinds that spin upward, in contrast to tornadoes that spin downward from the base of a cloud. The main difference between these two types of vortexes is that, while *landspouts* are formed below a supercell and travel upwards following a non-condensed vortex tube, *dust devils* typically form on clear days when warm air rises into cooler air above, which generates a vortex spinning from the ground upward. Our vorticity dynamics model can simulate different whirlwind phenomena not only at different scales but also made up of different types of matter: Condensed water in the atmosphere, debris trapped in vortex tubes, and dust. In particular, *dust devils* can be easily generated by our framework since we already simulate the turbulent flow of heat in the atmosphere. This is demonstrated in Figure 17, where we input wind-shear over a dusty terrain, generating a well-formed and short-lived whirlwind.

6.5 Tornado Life Cycle

We reproduce the process of tornadogenesis and tornado decay, as shown in Figure 21, by first setting up a mature thunderstorm, and, afterwards, let a wind-shear evolve so that the rotating cumulonimbus generates a tornado on its base. Once the non-local shear at the boundary ceases to exist, the tornado decays and gradually dissipates. Additionally, we are able to simulate the transition between tornado types, as shown in Figure 22, where a *wedge* tornado evolves into a *funnel* structure until it disappears since it lacks the energy to sustain the vortex field.

6.6 Mesoscale Cyclones

To evaluate the mesoscale counterpart of our scheme, we carry out different validation experiments of hurricane phenomena.

6.6.1 Gravity Waves. We simulate the formation of large-scale vortex phenomena generated by gravity waves in the atmosphere, as shown in Figure 18. Our framework is able to capture the initial stages of hurricane formation, including the transition from local disturbances to a sustained rotational field. As discussed before, our one-moment RANS formulation is able to handle dynamic boundaries with incoming impulses.

6.6.2 Hurricane Eye. Next, we focus on the very center of the hurricane, which enables us to visualize the so-called *hurricane eye.* This region of the cyclone, shown in Figure 19, using atmospheric profiles from hurricane *Diane* (which occurred in August 1995 and has been the first Atlantic hurricane to cause more than an estimated one billion in damage), consists of a roughly circular area surrounded by the *eyewall*, which is a ring of clouds that rotate about the vortex. Inside the eye, the pressure can be as low as to stop condensation, which enables the formation of relatively clear skies inside of it. A photographic comparison is also shown in Figure 20.

Quantitatively, we compute the angular velocity from the eye to the radius of maximum wind (RMW) along the pressure isosurface of 850 mb (around 1.5 km from the ground). We make two measurements: At $t = 0.5$ h and 3 h, respectively. As shown in Figure 24, our framework is able to reproduce the observed *regimes* of angular velocity for this hurricane event [Kossin and Eastin 2001]. Note, that we used multiple runs to account for the uncertainty in the measured profiles for this event. Moreover, in Figure 23, we compare one test run for this experiment using our direct vorticity update and the usual cross-product vorticity confinement as in Amador Herrera et al. [2021]. Our scheme produces less numerical dissipation, which is crucial for quantitative comparisons against observed data.

6.6.3 Sea Temperature. Finally, we analyzed the effect of surface sea temperature (SST) on the decay of hurricanes after landfall, i.e., when they hit land. For this, we generated four hurricane events with surface temperatures T_G from 26.85° C to 29.85° C, and measured their velocity profiles while traveling towards the land and decaying after hitting the coast. The results, depicted in Figure 25, show that, for greater levels of SST, the decay rate is slower, which means the hurricane is sustained for a longer time in land even after latent heat from the ocean has stopped fueling the vorticity of the cyclone. The values of hurricane decay obtained using our framework match the behaviour and value range of state-of-the-art data analysis [Fogarty et al. 2006; Li and Chakraborty 2020].

6.7 Weather Nowcasting

Finally, we streamed a full set of diverse atmospheric measurements (shear, temperature, pressure, and humidity) from weather radar

Fig. 15. Variations of different types of tornadoes simulated using our framework (top) and corresponding photo comparisons (bottom): *Rope* (a), *funnel* (b, c), *wedge* (d, e), *bowl-shape* (f), *landspout* (g), *multi-vortex* (h).

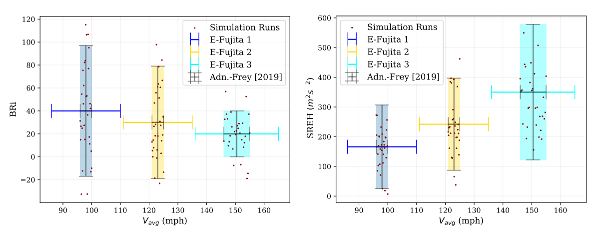

Fig. 16. We simulate thirty funnel tornado events per Fujita category, with varying velocities to match the velocity range of observed events. The correlations between tornado intensity with the Bulk Richardson Number (BRi) and Storm Relative Enviromental Helicity (SREH) match the real measurements of Anderson-Frey et al. [2019].

data[2] into our framework to simulate hurricane dynamics in real-time, enabling nowcasting. In particular, we simulated the time evolution of hurricane *Katrina* (August 2005), as demonstrated in Figure 1. Note, that for projecting this large-scale simulation onto the spherical surface of the earth, we streamed the different global atmospheric parameters as dynamic boundary conditions (see Section 5.2), and solved our RANS system on a co-moving mesh to reflect the translation of the center of rotation.

[2]Data taken from the www.ventusky.com service.

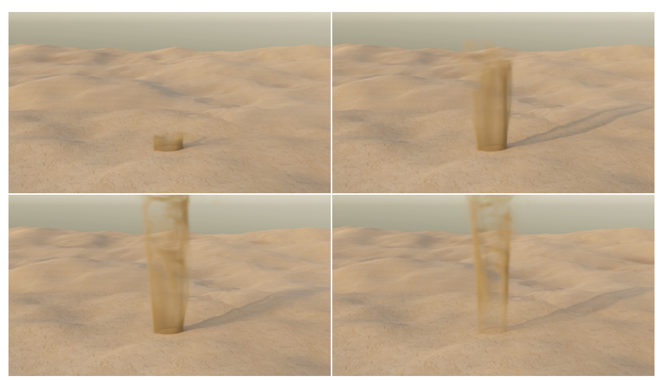

Fig. 17. Our vorticity dynamics scheme is able to simulate general vortex phenomena at different scales and within diverse contexts: Inside a supercell, from debris that got inside a vortex tube, and dust in the ground. In this simulation, a *dust devil* vortex (time evolution from left to right, top to bottom) is generated by the encounter of warm wind-shear with cool air in the atmosphere.

7 DISCUSSION

Our physically-based scheme describing the process of cyclogenesis enables the realistic simulation of multiple atmospheric vortex phenomena at different spatial and temporal scales. Note, that there are

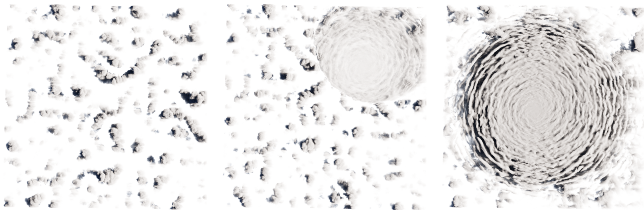

Fig. 18. Time evolution (from left to right) of an inlet gravity wave, from the top corner of the domain, which later evolves into a hurricane formation.

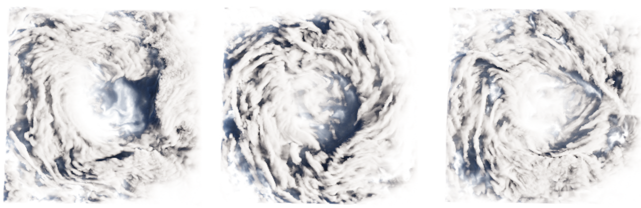

Fig. 19. One characteristic feature of mesoscale cyclones is the *hurricane eye* at the center of the vortex. Inside of this region, relatively weak winds and low pressure generate relatively clear skies.

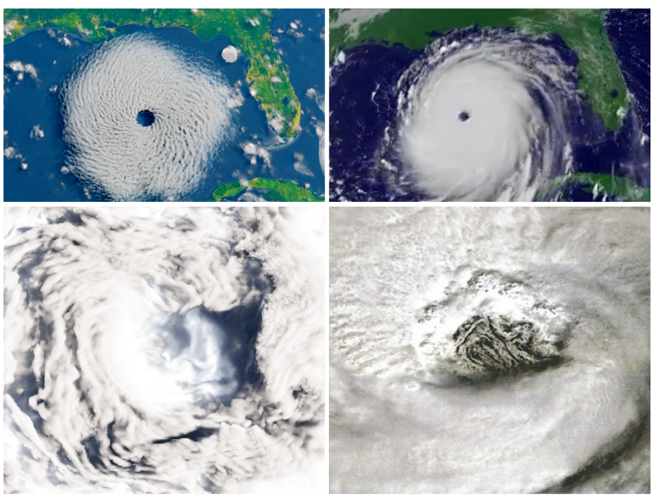

Fig. 20. Hurricane eye simulated using our hurricane module (left), and corresponding photo comparisons (right).

Fig. 21. Temporal evolution (from left to right) of the formation and subsequent decay of a *cone* tornado formed at the base of a rotating supercell.

many complex atmospheric models tailored for highly specialized computations of very specific weather phenomena and, while built based on principles from atmospheric science and fluid dynamics,

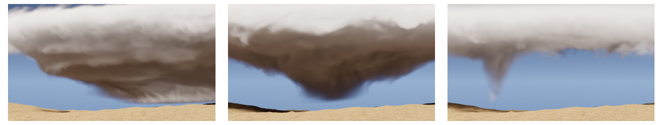

Fig. 22. Temporal evolution (from left to right) of a *wedge* tornado into a *funnel* geometry and its subsequent decay. Our principled approach for simulating tornadic phenomena enables us to reproduce the dynamic evolution and decay of tornadoes.

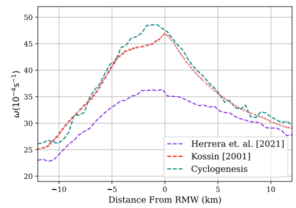

Fig. 23. We compare the angular velocity of hurricane *Diane* using our direct vorticity update (blue) and the cross-product confinement (purple) as in Amador Herrera et al. [2021]. Our model produces less numerical dissipation, which is an important factor for comparisons against real data.

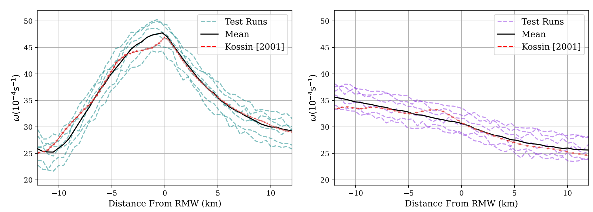

Fig. 24. For our simulation of the eye of hurricane *Diane*, we measure the angular velocity along the pressure isosurface of 850 mb from the eye (negative axis) to the radius of maximum wind (RMW), and further distances (positive axis). Both results, for $t = 0.5$ h (left) and $t = 3$ h (right), match the *eye regimes* observed by Kossin and Eastin [2001] for this hurricane event. We used multiple test runs with different boundary wind shears ($\pm 5\text{ms}^{-1}$) to account for the uncertainty in the measured shear profiles, and also plot the mean values.

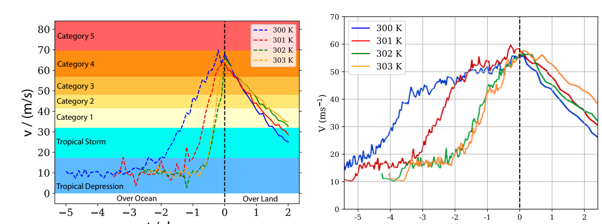

Fig. 25. We simulate multiple hurricane phenomena with different surface temperatures to measure the effect of SST on hurricane decay after striking land. Left: We find that greater SST generate cyclones that last longer on land. Right: Reproduction of the results obtained by Li and Chakraborty [2020] for reference. Our scheme is able to match the behaviour of highly specialized atmospheric circulation models.

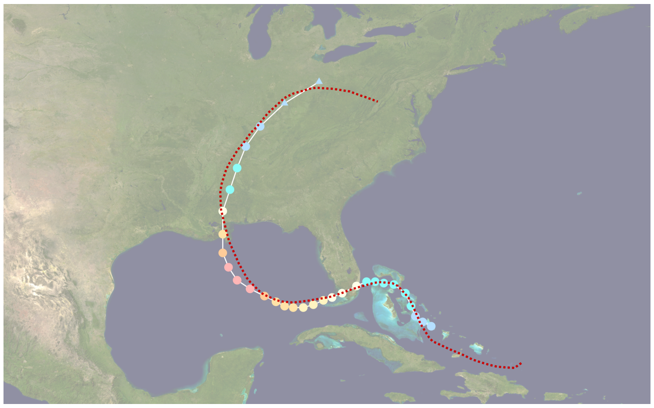

Fig. 26. Comparison of the path taken by hurricane *Katrina* (background map, points), as measured by the National Hurricane Center (NHC), and our simulation results (red path). Streaming real-time weather data into our framework allows us to enable nowcasting of real weather phenomena.

our model works under specific assumptions, modifications and coupling between processes in such a way that it encompasses a more general and efficient scheme for the turbulent transport of heat and water in the atmosphere, including different *hydrometeors*. The explicit parametrization of the underlying physical processes at play in vorticity dynamics and turbulent heat and water continuity enables us to capture the formation, development, and decay of vortex tubes at both supercell-scale and mesoscale. In turn, we are able to simulate diverse cyclonic phenomena, such as *multi-vortex* cyclones, *rope* tornadoes, and hurricanes, as well as reproducing the cyclogenesis of multiple types of tornadoes resulting from the rotation of a parent supercell, e.g., *wedge*, *funnel* and *bowl-shaped* tornadic phenomena. Additionally, our two-fluid coupling scheme is able to capture tornadic phenomena that occurs at regions where condensation is not present but where vorticity generates vortex tubes, e.g., during the formation of *dust devils*, *landspouts*, and the base of a *cone* tornado. Furthermore, our method captures the emergent dynamics of hurricanes, which can be used not only for reproducing key geometrical characteristics of these type of cyclones like, for instance, the *eye* of the hurricane, but also for analyzing the effects of different atmospheric and ground conditions on hurricane development and dissipation. Finally, our framework is able to generate hurricanes based on streamed weather data, enabling nowcasting. This provides a new way of interacting with real-world phenomena, in particular when used in virtual and augmented reality applications.

Limitations and Future Work. Our framework can be extended in various directions. First, multiple eyewalls may emerge within strong tropical cyclones, and under certain circumstances, the inner eyewall can even be replaced by an outer eyewall. This replacement cycle has not been addressed so far. Additionally, the ground plays an important role in our simulations in terms of boundary values for temperature, pressure, and water content, but it does not react to the velocity field. In particular, coupling interactive domains would enable us to more realistically capture the destructive character of strong vortex tubes. Moreover, other physical processes that play an important role in the development of atmospheric conditions could be explored and incorporated into our framework, e.g., vegetation feedback and lightning strikes. Finally, our cyclone scheme is limited to hurricanes with a single main rotation axis. It would be interesting to explore a more general formulation that would allow the simulation of mesoscale phenomena with multiple cyclones, e.g., the Fujiwhara Effect of colliding hurricanes.

8 CONCLUSION

We have proposed a novel physically-based model for the efficient and comprehensive simulation of turbulent phenomena in the atmosphere. Our approach explicitly models and integrates vorticity and turbulent multi-physics by parametrizing and coupling the underlying microphysical, fluid, and heat dynamics processes that generate vortexes at different scales. We have shown that our framework is capable of simulating the dynamic emergence, development, and dissipation of cyclonic phenomena, including different types of tornadoes and hurricane events. Furthermore, we have validated our scheme by performing multiple comparison experiments against both state-of-the-art and real data from storm soundings and radar technologies. The results of these validation experiments show that our scheme improves the visual simulation of cyclones and is able to reproduce similar results as those obtained from highly specialized atmospheric models, while still being a comprehensive and efficient framework that can be used for generating immersive virtual environments.

Future work in this direction includes exploring more complex hurricane dynamics that take into account the interaction of multiple eyewalls at the center of the hurricane, and the implementation of a more complex coupling between vortexes and the surrounding terrain. In this sense, it would be interesting to incorporate destructible domains that affect the dynamics of cyclones. Finally, there are multiple physical processes like vegetation feedback, lightning, etc., that we currently do not take into account but that play an important role in cyclonic phenomena. Integrating these effects into our framework would enable the simulation of more complex scenes.

A APPENDIX

A.1 Table of Symbols

Table 2 provides an overview of parameters and variables, including its numerical values and units, in order of appearance.

A.2 Tensor Notation

Using this notation, a tensor is represented by its indices, with the rule that a sum is performed for every repeating index. For instance, the dot product of two vectors $\boldsymbol{a}$ and $\boldsymbol{b}$ is written as $a_i b_i = a_1 b_1 + a_2 b_2 + a_3 b_3$. Other useful operations include the cross product, written as $c_i = \epsilon_{ijk} a_j b_k$, and matrix multiplication, which in this notation reads $C_{ij} = A_{ik} B_{kj}$, for matrices A and B. In the context of differential operators, the same rules apply for vectors of differentials. For instance, the divergence of a vector function $\boldsymbol{u}$ reads $\nabla \cdot \boldsymbol{u} = \partial u_i / \partial x_i$.

Table 2. List of different symbols (in order of appearance) used in our model and their typical values for simulation. Note that quantities without a shown value correspond to dynamic parameters computed at simulation time.

Symbol	Name	Value	Units
$\boldsymbol{x} = (x, y, z)$	Cartesian Coordinates	–	m
a	Hydrometeor Index: vapor v, rain r, etc.	–	–
q_a	Mixing Ratio of a	–	$\mathrm{kg\,kg^{-1}}$
T_G	Temperature at Ground Level	293.15	K
Γ_0	Lapse Rate	$-6.5 \cdot 10^{-3}$	$\mathrm{K\,m^{-1}}$
Γ_1	Second Lapse Rate	$6.5 \cdot 10^{-3}$	$\mathrm{K\,m^{-1}}$
z_1	Inversion Altitude	8000	m
p	Atmospheric Pressure	–	Pa
ρ_d	Density of Dry Air	2500	$\mathrm{kg\,m^{-3}}$
R_d	Gas Constant of Dry Air	0.287	$\mathrm{J\,K^{-1}g^{-1}}$
Π	Non-dimensional Pressure	–	1
p_G	Pressure at Ground Level	$1.013 \cdot 10^{8}$	Pa
θ_v	Virtual Potential Temperature	–	K
θ	Potential Temperature	–	K
$\boldsymbol{u}$	Wind Velocity	–	$\mathrm{ms^{-1}}$
μ	Dynamic Viscosity	1.465	$\mathrm{kg\,m^{-1}s^{-1}}$
ν_T	Turbulent Viscosity	–	$\mathrm{m^2s^{-1}}$
k	Turbulent Kinetic Energy	–	$\mathrm{m^2s^{-2}}$
s_k	Subgrid Scale	–	m
C_ϵ	Ventilation Coefficient	0.2	1
ν_M	Eddy Mixing	–	$\mathrm{m^2s^{-1}}$
C_e	Mixing Constant	0.1	1
B	Buoyancy Acceleration	–	$\mathrm{m\,s^{-2}}$
$\boldsymbol{\alpha}_{\text{cor}}$	Coriolis Term	$(0, 0.2, 0)$	$\mathrm{m\,s^{-2}}$
M_ϕ	Microphysical Phase Change	–	$\mathrm{kg\,kg^{-1}\,s^{-1}}$
D_ϕ	Microphysical Turbulent Term	–	$\mathrm{kg\,kg^{-1}\,s^{-1}}$
L_t	Latent Heat Index: fusion L_f, etc.	–	$\mathrm{kJ\,kg^{-1}}$
L_v	Latent Heat of Vaporization	2260	$\mathrm{kJ\,kg^{-1}}$
L_f	Latent Heat of Fusion	334	$\mathrm{kJ\,kg^{-1}}$
L_s	Latent Heat of Sublimation	2838	$\mathrm{kJ\,kg^{-1}}$
X_a	Mass Fraction of a	–	$\mathrm{kg\,kg^{-1}}$
ρ_{dust}	Dust Density	490	$\mathrm{kg\,m^{-3}}$
m_{dust}	Dust Mass	$7.5 \cdot 10^{-10}$	kg
r_{dust}	Dust Radius	$7.1 \cdot 10^{-5}$	m
ν_T	Dust Viscosity	1.285	$\mathrm{kg\,m^{-1}s^{-1}}$
c_k	Von Karman Constant	0.4	1
$\boldsymbol{x} = (r, \gamma, z)$	Cylindrical Coordinates	–	m
Φ	Earth's Geopotential	–	$\mathrm{m^2s^{-2}}$
h	Flux of Sensible Heat	–	$\mathrm{J\,m^{-2}\,s^{-1}}$
m	Vertical Flux of Moisture	–	$\mathrm{Kg\,m^{-2}\,s^{-1}}$
Q	Non-adiabatic Heating	–	J
B	Holland's Radial Parameter	0.5	1
$R_{\max}$	Maximum Storm Radius	150	km

A.3 Thermodynamic Variables

For comparing against real data, we compute two additional thermodynamic variables of storms. Specifically, the Bulk Richardson Number (BRi) and the Storm Relative Environmental Helicity (SREH). For the BRi, we simply use

$$\text{BRi} = \frac{(g/T_v)\,\theta_v \mathrm{d}z}{(\Delta U)^2 + (\Delta V)^2},$$

with gravity acceleration g, absolute temperature T, potential temperature θ_v, layer size $\mathrm{d}z$, and wind shear in the layer ΔU and ΔV. Following real measurements, we computed the BRi at the 1 km layer. For the environmental helicity, we compute

$$\text{SREH} = \int_0^h \left(\hat{\boldsymbol{k}} \frac{\partial ||\boldsymbol{W}||}{\partial z} \right) \cdot (\boldsymbol{W} - \tilde{\boldsymbol{u}})\, \mathrm{d}z,$$

with vertical unit vector $\hat{\boldsymbol{k}}$, wind shear $\boldsymbol{W}$, and storm velocity $\tilde{\boldsymbol{u}}$. Again, according to measurements, we integrate at an altitude of $h = 3$ km.

A.4 Discrete Differential Operators

The numerical discretization of our cyclogenesis model is performed using a staggered grid where the velocity fields of wind and dust, $\boldsymbol{u} = (u, v, w)$ and $\boldsymbol{u}_d = (u_d, v_d, w_w)$, respectively, are stored at the faces of each voxel, while all the other scalar quantities s (turbulent kinetic energy, mixing ratios, and potential temperature) as well as the vorticity $\boldsymbol{\omega}$ are stored at the center of the voxels, as demonstrated in Figure 27. Using this grid, we compute the discrete version of our model using centered finite differences. The divergence of the velocity fields is computed as

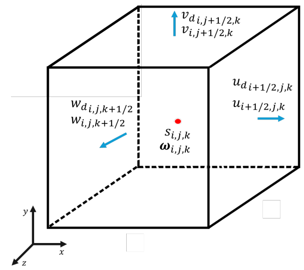

Fig. 27. Schematic representation of a single voxel from our staggered grid. We store the velocity components $\boldsymbol{u} = (u, v, w)$ and $\boldsymbol{u}_d = (u_d, v_d, w_d)$ at the faces (blue arrows), while all the other scalar quantities s, as well as the vorticity $\boldsymbol{\omega}$, are stored at the center (red point).

$$(\nabla \cdot \boldsymbol{u})_{i,j,k} \approx \frac{u_{i+1/2,j,k} - u_{i-1/2,j,k}}{\Delta x} + \frac{v_{i,j+1/2,k} - v_{i,j-1/2,k}}{\Delta y} + \frac{w_{i,j,k+1/2} - w_{i,j,k-1/2}}{\Delta z},$$

where Δx, Δy, and Δz are the mesh step sizes in each dimension. Additionally, the gradient of scalar quantities is given by

$$\left(\frac{\partial s}{\partial x}\right)_{i+1/2,j,k} = \frac{s_{i+1,j,k} - s_{i-1,j,k}}{\Delta x},$$
$$\left(\frac{\partial s}{\partial y}\right)_{i,j+1/2,k} = \frac{s_{i,j+1,k} - s_{i,j-1,k}}{\Delta y},$$
$$\left(\frac{\partial s}{\partial z}\right)_{i,j,k+1/2} = \frac{s_{i,j,k+1} - s_{i,j,k-1}}{\Delta z}.$$

Finally, for the discrete curl of the velocity we compute

$$(\nabla \times \boldsymbol{u})_{i,j,k} = \Bigg(\frac{w_{i,j+1,k} - w_{i,j-1,k}}{2\Delta y} - \frac{v_{i,j,k+1} - v_{i,j,k-1}}{2\Delta z}, \frac{u_{i,j,k+1} - u_{i,j,k-1}}{2\Delta z} - \frac{w_{i+1,j,k} - w_{i-1,j,k}}{2\Delta x}, \frac{v_{i+1,j,k} - v_{i-1,j,k}}{2\Delta x} - \frac{u_{i,j+1,k} - u_{i,j-1,k}}{2\Delta y} \Bigg),$$

where the velocity components at the center are computed by averaging the values at the faces, such that

$$\boldsymbol{u}_{i,j,k} = \Bigg(\frac{u_{i-1/2,j,k} + u_{i+1/2,j,k}}{2}, \frac{v_{i,j-1/2,k} + v_{i,j+1/2,k}}{2}, \frac{w_{i,j,k-1/2} + w_{i,j,k+1/2}}{2} \Bigg).$$

REFERENCES

G. Alfonsi. 2009. Reynolds-averaged Navier–Stokes equations for turbulence modeling. *Applied Mechanics Reviews* 62, 4 (2009).

J. A. Amador Herrera, T. Hädrich, W. Pałubicki, D. T. Banuti, S. Pirk, and D. L. Michels. 2021. Weatherscapes: Nowcasting Heat Transfer and Water Continuity. *ACM Transaction on Graphics* 40, 6, Article 204 (12 2021).

A. K. Anderson-Frey, Y. P. Richardson, A. R. Dean, R. L. Thompson, and B. T. Smith. 2019. Characteristics of tornado events and warnings in the southeastern United States. *Weather and Forecasting* 34, 4 (2019), 1017–1034.

A. Bouthors and F. Neyret. 2004. Modeling clouds shape. In *Eurographics 2004–Short Presentations*, M. Alexa and E. Galin (Eds.). Eurographics Association.

J. R. Colquhoun and P. A. Riley. 1996. Relationships between tornado intensity and various wind and thermodynamic variables. *Weather and forecasting* 11, 3 (1996), 360–371.

W. Cui and L. Caracoglia. 2019. A new stochastic formulation for synthetic hurricane simulation over the North Atlantic Ocean. *Engineering Structures* 199 (2019), 109597.

D. Demidov. 2019. AMGCL: An Efficient, Flexible, and Extensible Algebraic Multigrid Implementation. *Lobachevskii Journal of Mathematics* 40, 5 (01 May 2019), 535–546. https://doi.org/10.1134/S1995080219050056

X. Ding. 2005. *Physically-based Simulation of Tornadoes.* Master's thesis. University of Waterloo.

T. N. Dobashi, Tsuyoshi Yamamoto. 2002. Interactive Rendering of Atmospheric Scattering Effects Using Graphics Hardware. (2002).

Y. Dobashi, K. Kaneda, H. Yamashita, T. Okita, and T. Nishita. 2000. A simple, efficient method for realistic animation of clouds. In *Proceedings of the 27th annual conference on Computer graphics and interactive techniques.* 19–28.

H. Doleisch, P. Muigg, and H. Hauser. 2004. Interactive visual analysis of hurricane isabel with simvis. *IEEE Visualization Contest* (2004).

W. M. Drennan, J. A. Zhang, J. R. French, C. McCormick, and P. G. Black. 2007. Turbulent fluxes in the hurricane boundary layer. Part II: Latent heat flux. *Journal of the atmospheric sciences* 64, 4 (2007), 1103–1115.

K. K. Droegemeier and R. B. Wilhelmson. 1985. Three-dimensional numerical modeling of convection produced by interacting thunderstorm outflows. Part I: Control simulation and low-level moisture variations. *Journal of the atmospheric sciences* 42, 22 (1985), 2381–2403.

C. W. Ferreira Barbosa, Y. Dobashi, and T. Yamamoto. 2015. Adaptive Cloud Simulation Using Position Based Fluids. *Comput. Animat. Virtual Worlds* 26, 3–4 (2015), 367–375.

C. T. Fogarty, R. J. Greatbatch, and H. Ritchie. 2006. The role of anomalously warm sea surface temperatures on the intensity of Hurricane Juan (2003) during its approach to Nova Scotia. *Monthly weather review* 134, 5 (2006), 1484–1504.

S. Gao, S. Jia, Y. Wan, T. Li, S. Zhai, and X. Shen. 2019. The role of latent heat flux in tropical cyclogenesis over the Western North Pacific: Comparison of developing versus non-developing disturbances. *Journal of Marine Science and Engineering* 7, 2 (2019), 28.

I. Garcia-Dorado, D. G. Aliaga, S. Bhalachandran, P. Schmid, and D. Niyogi. 2017. Fast Weather Simulation for Inverse Procedural Design of 3D Urban Models. *ACM Trans. Graph.* 36, 2, Article Article 21 (2017), 19 pages.

G. Y. Gardner. 1985. Visual Simulation of Clouds. In *Proceedings of the 12th Annual Conference on Computer Graphics and Interactive Techniques (SIGGRAPH '85)*. Association for Computing Machinery, 297–304.

C. Gissler, A. Henne, S. Band, A. Peer, and M. Teschner. 2020. An Implicit Compressible SPH Solver for Snow Simulation. *ACM Trans. Graph.* 39, 4, Article 36 (2020), 16 pages.

P. Goswami and F. Neyret. 2017. Real-Time Landscape-Size Convective Clouds Simulation and Rendering. In *Proceedings of the 13th Workshop on Virtual Reality Interactions and Physical Simulations (VRIPHYS '17).* Eurographics Association, 1–8.

E. J. Griffith, F. H. Post, T. Heus, and H. J. J. Jonker. 2009. *Interactive simulation and visualisation of atmospheric large-eddy simulations.* Technical Report. Technical Report 2 TuDelft Data Visualization Group.

T. Hädrich, D. T. Banuti, W. Pałubicki, S. Pirk, and D. L. Michels. 2021. Fire in Paradise: Mesoscale Simulation of Wildfires. *ACM Trans. on Graph.* 40, 4, Article 163 (2021).

T. Hädrich, M. Makowski, W. Pałubicki, D. T. Banuti, S. Pirk, and D. L. Michels. 2020. Stormscapes: Simulating Cloud Dynamics in the Now. *ACM Transaction on Graphics* 39, 6, Article 175 (12 2020).

M. J. Harris, W. V. Baxter, T. Scheuermann, and A. Lastra. 2003. Simulation of Cloud Dynamics on Graphics Hardware. In *ACM SIGGRAPH/EUROGRAPHICS Conference on Graphics Hardware (HWWS '03)*. Eurographics Association, 92–101.

G. J. Holland. 1980. An analytic model of the wind and pressure profiles in hurricanes. (1980).

G. J. Holland and R. T. Merrill. 1984. On the dynamics of tropical cyclone structural changes. *Quarterly Journal of the Royal Meteorological Society* 110, 465 (1984), 723–745.

R. A. Houze. 2014. *Cloud Dynamics.* Elsevier.

ISO. 1975. Standard Atmosphere. *International Organization for Standardization* 2533 (1975).

T. Kajishima and K. Taira. 2016. *Computational fluid dynamics: incompressible turbulent flows.* Springer.

J. T. Kajiya and B. P. Von Herzen. 1984. Ray Tracing Volume Densities. *SIGGRAPH Comput. Graph.* 18, 3 (1984), 165–174.

J. D. Kepert. 2010. Tropical cyclone structure and dynamics. *Global perspectives on Tropical cyclones: from science to mitigation* (2010), 3–53.

J. B. Klemp. 1987. Dynamics of tornadic thunderstorms. *Annual review of fluid mechanics* 19, 1 (1987), 369–402.

J. P. Kossin and M. D. Eastin. 2001. Two distinct regimes in the kinematic and thermodynamic structure of the hurricane eye and eyewall. *Journal of the atmospheric sciences* 58, 9 (2001), 1079–1090.

H.-L. Kuo. 1965. On formation and intensification of tropical cyclones through latent heat release by cumulus convection. *Journal of the atmospheric sciences* 22, 1 (1965), 40–63.

L. Li and P. Chakraborty. 2020. Slower decay of landfalling hurricanes in a warming world. *Nature* 587, 7833 (2020), 230–234.

S. Liu, Z. Wang, Z. Gong, and Q. Peng. 2007. Real time simulation of a tornado. *The Visual Computer* 23, 8 (2007), 559–567.

S.-g. Liu, Z.-y. Wang, Z. Gong, F.-f. Chen, and Q.-s. Peng. 2006. Physically based modeling and animation of tornado. *Journal of Zhejiang University-SCIENCE A* 7, 7 (2006), 1099–1106.

J. Luo, A. P. Makwana, D. Liao, and J. P. Kincaid. 2008. Hurricane!-a simulation-based program for science education. In *2008 Winter Simulation Conference.* IEEE, 2543–2548.

G. L. Mellor and T. Yamada. 1974. A hierarchy of turbulence closure models for planetary boundary layers. *Journal of the atmospheric sciences* 31, 7 (1974), 1791–1806.

M. M. Miglietta, J. Mazon, and R. Rotunno. 2017. Numerical simulations of a tornadic supercell over the Mediterranean. *Weather and Forecasting* 32, 3 (2017), 1209–1226.

R. Miyazaki, Y. Dobashi, and T. Nishita. 2002. Simulation of Cumuliform Clouds Based on Computational Fluid Dynamics. In *Eurographics.*

R. Miyazaki, S. Yoshida, Y. Dobashi, and T. Nishita. 2001. A method for modeling clouds based on atmospheric fluid dynamics. In *Proceedings Ninth Pacific Conference on Computer Graphics and Applications. Pacific Graphics 2001.* IEEE, 363–372.

C.-H. Moeng. 1984. A large-eddy-simulation model for the study of planetary boundary-layer turbulence. *Journal of the Atmospheric Sciences* 41, 13 (1984), 2052–2062.

F. Neyret. 1997. Qualitative Simulation of Convective Cloud Formation and Evolution. In *Computer Animation and Simulation '97.* 113–124.

T. Nishita, Y. Dobashi, and E. Nakamae. 1996. Display of clouds taking into account multiple anisotropic scattering and sky light. In *Proceedings of the 23rd annual conference on Computer graphics and interactive techniques.* 379–386.

L. Orf. 2019. A violently tornadic supercell thunderstorm simulation spanning a quarter-trillion grid volumes: Computational challenges, I/O framework, and visualizations of tornadogenesis. *Atmosphere* 10, 10 (2019), 578.

L. Orf, R. Wilhelmson, B. Lee, C. Finley, and A. Houston. 2017. Evolution of a long-track violent tornado within a simulated supercell. *Bulletin of the American Meteorological Society* 98, 1 (2017), 45–68.

D. Overby, Z. Melek, and J. Keyser. 2002. Interactive physically-based cloud simulation. In *Proceedings of Pacific Graphics.* 469–470.

W. Pałubicki, M. Makowski, W. Gajda, T. Hädrich, , , D. L. Michels, and S. Pirk. 2022. Ecoclimates: Climate-response Modeling of Vegetation. *ACM Trans. Graph.* 41, 4, Article 1 (July 2022), 19 pages.

L. Peng and H. Kuo. 1975. A numerical simulation of the development of tropical cyclones. *Tellus* 27, 2 (1975), 133–144.

N. Pilguj, M. Taszarek, Ł. Pajurek, and M. Kryza. 2019. High-resolution simulation of an isolated tornadic supercell in Poland on 20 June 2016. *Atmospheric Research* 218 (2019), 145–159.

W. Raateland, T. Hädrich, J. A. A. Herrera, D. T. Banuti, W. Pałubicki, S. Pirk, K. Hildebrandt, and D. L. Michels. 2022. DCGrid: An Adaptive Grid Structure for Memory-Constrained Fluid Simulation on the GPU. *Proc. ACM Comput. Graph. Interact. Tech.* 5, 1, Article 3 (May 2022), 14 pages.

E. B. Rodgers, W. S. Olson, V. M. Karyampudi, and H. F. Pierce. 1998. Satellite-derived latent heating distribution and environmental influences in Hurricane Opal (1995). *Monthly weather review* 126, 5 (1998), 1229–1247.

R. Rotunno and J. Klemp. 1985. On the rotation and propagation of simulated supercell thunderstorms. *Journal of Atmospheric Sciences* 42, 3 (1985), 271–292.

J. Schalkwijk, H. J. J. Jonker, A. P. Siebesma, and E. Van Meijgaard. 2015. Weather forecasting using GPU-based large-eddy simulations. *Bulletin of the American Meteorological Society* 96, 5 (2015), 715–723.

A. Selle, R. Fedkiw, B. Kim, Y. Liu, and J. Rossignac. 2008. An unconditionally stable MacCormack method. *Journal of Scientific Computing* 35 (2008), 350–371.

R. Sheets. 1982. On the structure of hurricanes as revealed by research aircraft data. In *Intense atmospheric vortices.* Springer, 35–49.

J. Stam. 1999. Stable Fluids. *Proc. of ACM SIGGRAPH* (1999), 121–128.

H. T. Taylor, B. Ward, M. Willis, and W. Zaleski. 2010. The saffir-simpson hurricane wind scale. *Atmospheric Administration: Washington, DC, USA* (2010).

P. J. Vickery, P. Skerlj, A. Steckley, and L. Twisdale. 2000. Hurricane wind field model for use in hurricane simulations. *Journal of Structural Engineering* 126, 10 (2000), 1203–1221.

U. Vimont, J. Gain, M. Lastic, G. Cordonnier, B. Abiodun, and M.-C. Cani. 2020. Interactive Meso-scale Simulation of Skyscapes. *Eurographics* (2020).

A. Webanck, Y. Cortial, E. Guérin, and E. Galin. 2018. Procedural cloudscapes. In *Computer Graphics Forum*, Vol. 37. Wiley Online Library, 431–442.